$K^*(892)^0$ and $\phi(1020)$ production in Pb-Pb collisions at $\sqrt{s_{NN}} = 2.76$ TeV

B. Abelev *et al.*[*]

(ALICE Collaboration)

The yields of the $K^*(892)^0$ and $\phi(1020)$ resonances are measured in Pb-Pb collisions at $\sqrt{s_{NN}} = 2.76$ TeV through their hadronic decays using the ALICE detector. The measurements are performed in multiple centrality intervals at mid-rapidity ($|y| < 0.5$) in the transverse-momentum ranges $0.3 < p_T < 5$ GeV/c for the $K^*(892)^0$ and $0.5 < p_T < 5$ GeV/c for the $\phi(1020)$. The yields of $K^*(892)^0$ are suppressed in central Pb-Pb collisions with respect to pp and peripheral Pb-Pb collisions (perhaps due to rescattering of its decay products in the hadronic medium), while the longer-lived $\phi(1020)$ meson is not suppressed. These particles are also used as probes to study the mechanisms of particle production. The shape of the p_T distribution of the $\phi(1020)$ meson, but not its yield, is reproduced fairly well by hydrodynamic models for central Pb-Pb collisions. In central Pb-Pb collisions at low and intermediate p_T, the $p/\phi(1020)$ ratio is flat in p_T, while the p/π and $\phi(1020)/\pi$ ratios show a pronounced increase and have similar shapes to each other. These results indicate that the shapes of the p_T distributions of these particles in central Pb-Pb collisions are determined predominantly by the particle masses and radial flow. Finally, $\phi(1020)$ production in Pb-Pb collisions is enhanced, with respect to the yield in pp collisions and the yield of charged pions, by an amount similar to the Λ and Ξ.

I. INTRODUCTION

Ultrarelativistic heavy-ion collisions are expected to produce a hot and dense state of matter, the quark-gluon plasma [1–3]. At a critical temperature of $T_c \approx 160$ MeV [3–5] a crossover transition between the partonic (i.e., a system with deconfined quarks) and hadronic phases is expected to take place. Statistical models [6–13] have been successfully applied to particle yields in order to estimate the values of the chemical freeze-out temperature and the baryochemical potential. However, resonance yields may deviate from the values expected from thermal models due to hadronic processes (rescattering and regeneration) that might change the reconstructible resonance yields even after chemical freeze-out. Resonance yields may be regenerated through pseudoelastic scattering, in which particles scatter through a resonance state [e.g., $\pi^- K^+ \rightarrow K^*(892)^0 \rightarrow \pi^- K^+$ and $K^- K^+ \rightarrow \phi(1020) \rightarrow K^- K^+$] [14–16]. Pseudoelastic scattering does not change the abundances of the scattered particles, but may increase the measured yield of the resonance state through which they scattered. If a resonance has a short enough lifetime, it may decay during the hadronic phase and its decay products may undergo elastic or pseudoelastic scatterings. Information about the resonance may be lost if at least one of its decay products elastically scatters in the hadronic medium or undergoes pseudoelastic scattering via a different resonance state [e.g., a pion from a $K^*(892)^0$ decay scatters with another pion, $\pi^- \pi^+ \rightarrow \rho(770)^0 \rightarrow \pi^- \pi^+$] [17]. The net effect of pseudoelastic scattering on the yield of a resonance will depend on whether regeneration of that resonance is outweighed by rescattering of its decay products through other resonances. In the case of the $K^*(892)^0$, the πK interaction cross section [18] is smaller than the $\pi \pi$ cross section [19], so rescattering may dominate and the measured $K^*(892)^0$ yield may be smaller than the yield at chemical freeze-out. Calculations using ultrarelativistic quantum molecular dynamics (UrQMD) [20,21] predict that both regeneration and rescattering affect the resonance yields predominantly for transverse momenta $p_T \lesssim 2$ GeV/c [14,17]. The final reconstructible resonance yields depend on the chemical freeze-out temperature, the scattering cross sections of its decay products, and the timescale during which rescattering and regeneration are active in the hadronic phase, i.e., the time between chemical and kinetic freeze-out. The model described in Refs. [15,22,23] combines thermal-model calculations with rescattering effects in the hadronic phase. It predicts the ratios of (p_T-integrated) resonance yields to the yields of stable particles as a function of both the chemical freeze-out temperature and the lifetime of the hadronic phase. While this model was derived for a Relativistic Heavy Ion Collider (RHIC) collision energy ($\sqrt{s_{NN}} = 130$ GeV), its predictions span a wide range of freeze-out temperatures and hadronic lifetimes and remain valid at Large Hadron Collider (LHC) energies.

Chiral symmetry is expected to be restored [24] above the chiral transition temperature; resonances that decay when chiral symmetry was at least partially restored are expected to exhibit mass shifts and/or width broadening [25–28]. Regeneration of resonances in the late hadronic phase increases the fraction of resonances with vacuum masses and widths and may inhibit the observation of the signatures of chiral symmetry restoration. Since model calculations indicate that rescattering and regeneration modify the resonance signal more strongly for $p_T \lesssim 2$ GeV/c, signatures of chiral symmetry may be difficult to observe in the case of low-p_T resonances which are reconstructed via hadronic decays.

---

[*]Full author list given at the end of the article.

This article presents measurements of the $K^*(892)^0$, $\overline{K}^*(892)^0$, and $\phi(1020)$ mesons performed in multiple centrality intervals for Pb-Pb collisions at $\sqrt{s_{NN}} = 2.76$ TeV using the ALICE detector. The focus here is on low and intermediate p_T [$0.3 < p_T < 5$ GeV/c for the $K^*(892)^0$ and $0.5 < p_T < 5$ GeV/c for the $\phi(1020)$] and the integrated yields; results for high p_T will be presented in a future article. All measurements of the $K^*(892)^0$ and $\overline{K}^*(892)^0$ are averaged and these mesons are collectively referred to as K^{*0}. The $\phi(1020)$ meson is referred to as ϕ. The ALICE detector is described in Sec. II, with the emphasis on the subdetectors used in this analysis. The data-analysis procedure is described in Secs. III–V. Results, including resonance yields, masses, widths, mean transverse momenta, ratios to nonresonances, comparisons to predicted p_T distributions, and the ϕ enhancement ratio are presented in Sec. VI.

II. ALICE EXPERIMENT

A comprehensive description of the ALICE detector can be found in Ref. [29]. The main detector components used in this analysis are the V0 detector, the Inner Tracking System (ITS), and the Time Projection Chamber (TPC), which are located inside a 0.5 T solenoidal magnetic field. The V0 detector [30] consists of two scintillator hodoscopes placed on either side of the interaction point covering the pseudorapidity ranges $-3.7 < \eta < -1.7$ and $2.8 < \eta < 5.1$. A combination of hits in the V0 detector and the two innermost layers of the ITS is used is used as a minimum-bias trigger for Pb-Pb collisions [31]. Collision centrality is determined by using the multiplicity measured in the V0 detector along with Glauber-model simulations to describe the multiplicity distribution as a function of the impact parameter [31,32]. These simulations give $\langle N_{\mathrm{part}} \rangle$, the mean number of nucleons which participated in collisions in a given centrality interval. The ITS is made up of six cylindrical layers of silicon detectors with radii between 3.9 and 43 cm from the beam axis, covering the full azimuth. The pseudorapidity range $|\eta| < 0.9$ is covered by all six layers, with some of the individual layers covering larger ranges in pseudorapidity. The TPC [33], which is the main tracking detector, is a large cylindrical drift detector that covers the pseudorapidity range $|\eta| < 0.9$ with full azimuthal acceptance. Multiwire proportional chambers with cathode pad readout are arranged in 159 pad rows located at the ends of the TPC. Hits in the ITS and TPC are used to reconstruct charged particle tracks, which are used in the final determination of the primary collision vertex. The position resolution for the primary vertex in both the longitudinal direction and the transverse plane is ~ 10 μm for heavy-ion collisions. The TPC is also used to identify particles through their dE/dx (specific energy loss) in the TPC gas. The value of dE/dx is calculated using a truncated-mean procedure in which the average is evaluated using only the 60% of points with the lowest dE/dx values measured along a given track. The measured dE/dx is then compared to the expected dE/dx for a given particle species using a Bethe-Bloch parametrization. The deviation from the expected dE/dx value is expressed in units of the energy-loss resolution σ_{TPC}, which is 5% for isolated tracks

and 6.5% for central collisions [34]. The TPC allows kaons to be distinguished from pions for momenta $p < 0.7$ GeV/c and (anti)protons to be distinguished from pions and kaons for $p < 1$ GeV/c (with a separation power of 2σ in both cases).

III. EVENT AND TRACK SELECTION

The yields of K^{*0} and ϕ mesons are measured in about 13 million Pb-Pb collisions recorded in 2010 in the 0–90% centrality interval. The position of the primary vertex along the beam axis is required to be within 10 cm of the center of the ALICE detector. The K^{*0} and ϕ mesons are identified by reconstruction of their respective hadronic decays: $K^{*0} \to \pi^{\pm} K^{\mp}$ (branching ratio 0.666) and $\phi \to K^- K^+$ (branching ratio 0.489) [35]. The lifetimes in the vacuum of the K^{*0} and ϕ are 4.16 ± 0.05 fm/c and 46.3 ± 0.4 fm/c, respectively [35]. High-quality tracks are selected by requiring at least 70 reconstructed TPC clusters out of a possible 159 and requiring that the χ^2 per cluster of the reconstructed tracks be less than 4. Track momenta and pseudorapidity are restricted to the ranges $p_T > 150$ MeV/c and $|\eta| < 0.8$, respectively. To reduce the number of secondary particles from weak decays, each track is required to have at least one hit in the innermost layer of the ITS and a small distance of closest approach (DCA) to the primary vertex in the xy plane: $\mathrm{DCA}_{xy} < (0.0182 + 0.035 p_T^{-1.01})$ cm. The distance of closest approach in the z direction is also restricted: $\mathrm{DCA}_z < 2$ cm. The DCA_z cut is wider not because of the vertex resolution (which is similar for the longitudinal and transverse directions), but because of the tracking resolution, which is less precise for the z direction than the transverse plane. This is because the positions of points in the Silicon Pixel Detector (the innermost part of the ITS) are determined more precisely in the xy plane. The wide DCA_z cut is intended to remove particles that are highly displaced from the vertex. Finally, in the K^{*0} and ϕ analyses, pion and kaon tracks are required to be within $2\sigma_{\mathrm{TPC}}$ of the expected dE/dx values for each particle species.

IV. SIGNAL EXTRACTION

The K^{*0} and ϕ resonances are reconstructed through their invariant mass via identified decay-product candidates. For each centrality and p_T interval, the invariant-mass distribution of pairs of unlike-charge resonance decay products from the same event is constructed [as an example, see Figs. 1 and 2, panels (a) and (c)]. It is required that the rapidity of the pair lies within the range $|y_{\mathrm{pair}}| < 0.5$. In the construction of the K^{*0} invariant-mass distributions, it is possible that a track will be designated as both a pion candidate and a kaon candidate because it passes both identification cuts (especially at high p_T). In this event, such a track is assigned the kaon mass for some pairs and the pion mass for other pairs. First, the track will be assigned the kaon mass and pairs will be formed with each of the pion candidate tracks. Then the track will be assigned the pion mass and paired with each of the kaon candidates. (The track will never be paired with itself.) The K^{*0}
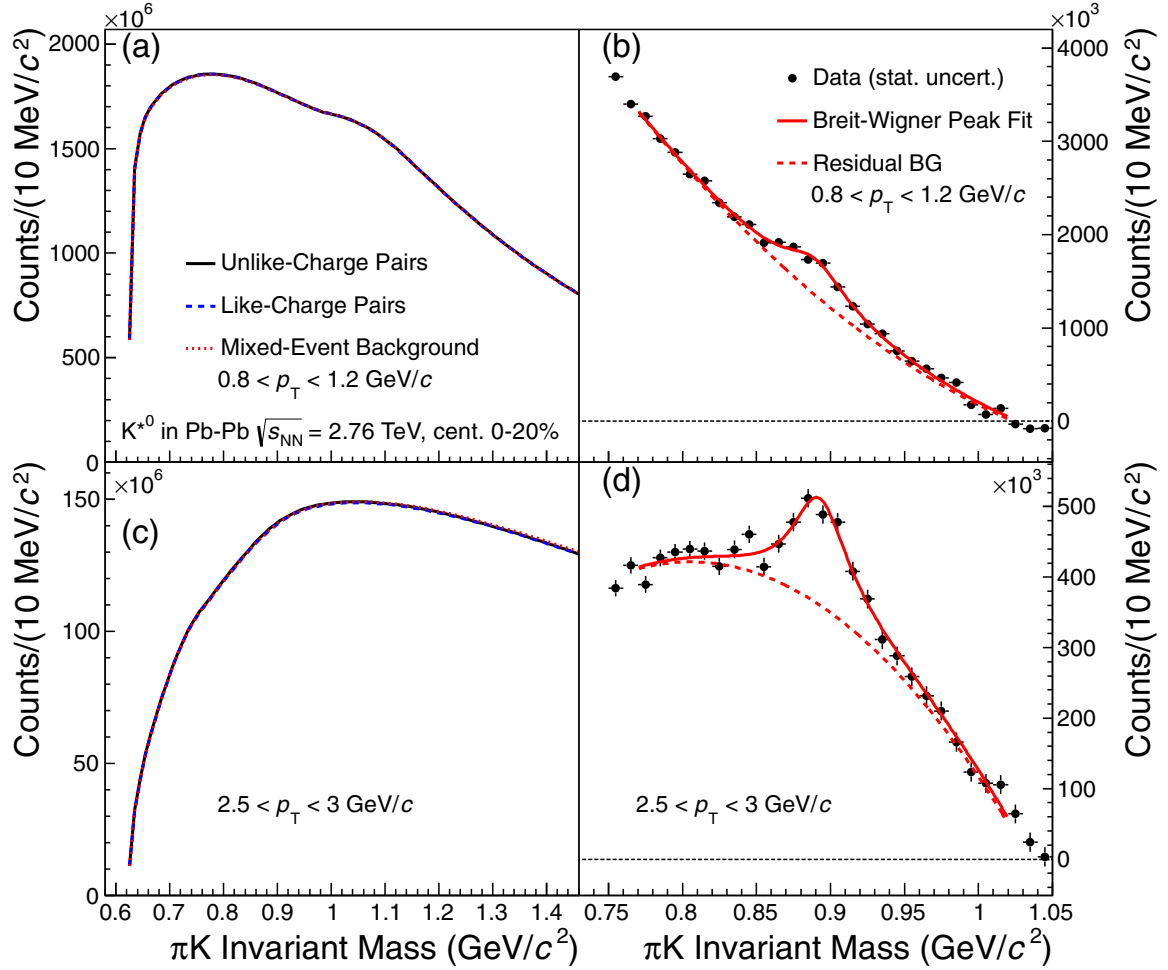
FIG. 1. (Color online) Example invariant-mass distributions for the K^{*0} in the 0–20% centrality interval in two p_T ranges: $0.8 < p_T < 1.2$ GeV/c [panels (a) and (b)] and $2.5 < p_T < 3$ GeV/c [panels (c) and (d)]. Panels (a) and (c) show the unlike-charge invariant-mass distributions for K^{*0} with combinatorial backgrounds. The normalized mixed-event combinatorial background is within 0.5% (0.7%) of the unlike-charge distribution for the low (high) p_T bin over the invariant-mass range shown here. The statistical uncertainties are not visible given the vertical scale. Panels (b) and (d) show the invariant-mass distributions after subtraction of the mixed-event background (plotted with statistical uncertainties) with fits to describe the peaks of the K^{*0} (solid curves) and residual backgrounds (dashed curves). In the interval $0.8 < p_T < 1.2$ GeV/c ($2.5 < p_T < 3$ GeV/c), the uncorrected K^{*0} yield is 7.4 (2.4) million, or 2.4 (0.80) per event; the signal-to-background ratio is 1.1×10^{-4} (5.6×10^{-4}) and the significance of the K^{*0} peak is 17 (25).

(ϕ) peak has a signal-to-background ratio[1] that ranges from 1.1×10^{-4} (1.4×10^{-3}) to 0.049 (1.7), depending on the p_T interval analyzed. For the full p_T range and centrality 0–80%, the K^{*0} (ϕ) peak has a signal-to-background ratio of 2.7×10^{-4} (4.4×10^{-3}).

The combinatorial background is estimated with an event-mixing technique by forming pairs using particles from different events. Each decay-product candidate track is combined with tracks from five other events to build uncorrelated pairs. Events for mixing are grouped based on the following similarity criteria: the difference in the vertex z position is less than 2 (5) cm for the K^{*0} (ϕ) and the difference in the

centrality percentile is required to be less than 10%. For the K^{*0} analysis, the difference in the event plane azimuthal angles between the two events is required to be less than 30°. The signal-to-background ratio is lower for the K^{*0} than the ϕ and the residual background for the K^{*0} also tends to have a larger slope or greater curvature than for the ϕ. For these reasons, and in order to provide a mixed-event combinatorial background which is a good representation of the true combinatorial background, the event mixing similarity criteria are somewhat stricter for the K^{*0}. The K^{*0} mixed-event combinatorial background is normalized such that its integral in the region of $1.1 < m_{\pi K} < 1.3$ GeV/c^2 is the same as the integral of the unlike-charge distribution over the same interval. The ϕ mixed-event combinatorial background is normalized to a region that surrounds, but excludes, the ϕ peak ($1 < m_{KK} < 1.01$ GeV/c^2 and $1.03 < m_{KK} < 1.06$ GeV/c^2). The boundaries of the normalization regions are changed and the resulting variations

---

[1]The signal-to-background ratio is evaluated by comparing the integrals of the signal and background over the ranges $0.77 < m_{\pi K} < 1.02$ GeV/c^2 for the K^{*0} and $1.01 < m_{KK} < 1.03$ GeV/c^2 for the ϕ.
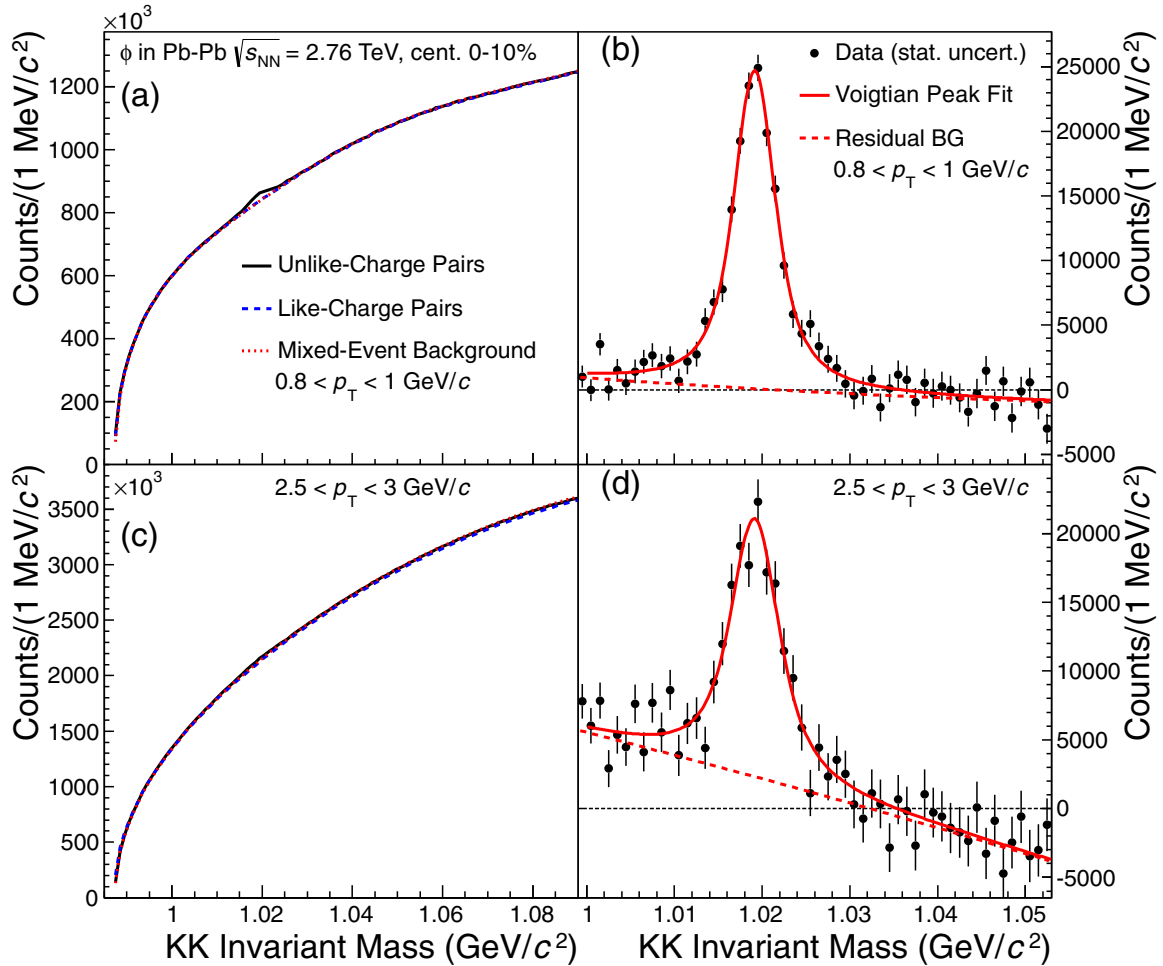
FIG. 2. (Color online) Example invariant-mass distributions for the ϕ in the 0–10% centrality interval in two p_T ranges: $0.8 < p_T < 1$ GeV/c [panels (a) and (b)] and $2.5 < p_T < 3$ GeV/c [panels (c) and (d)]. Panels (a) and (c) show the unlike-charge invariant-mass distributions for ϕ with combinatorial backgrounds. The normalized mixed-event combinatorial background is within 0.5% (1%) of the unlike-charge distribution for the low (high) p_T bin over most of the invariant-mass range shown here (with the exception of the ϕ peak itself and $m_{KK} < 0.995$ GeV/c^2). The statistical uncertainties are not visible given the vertical scale. Panels (b) and (d) show the invariant-mass distributions after subtraction of the mixed-event background (plotted with statistical uncertainties) with fits to describe the peaks of the ϕ (solid curves) and residual backgrounds (dashed curves). In the interval $0.8 < p_T < 1$ GeV/c ($2.5 < p_T < 3$ GeV/c), the uncorrected ϕ yield is 174 000 (149 000), or 0.11 (0.095) per event; the signal-to-background ratio is 0.01 (0.0035) and the significance of the ϕ peak is 38 (21).

in the experimental results (e.g., average values of 2.2% for the K^{*0} yield and 0.4% for the ϕ yield) are incorporated into the systematic uncertainties (see "Combinatorial background" in Table I). The combinatorial background is also estimated from the invariant-mass distribution of like-charge pairs from the same event. However, the resulting yields have larger statistical uncertainties and larger bin-to-bin fluctuations than the mixed-event background; the latter is therefore used for this analysis. Due to its lower signal-to-background ratio, the analysis of the K^{*0} is performed in four centrality intervals from 0–80%, while the ϕ analysis is performed in narrower centrality intervals.

After the normalized combinatorial background has been subtracted from the unlike-charge distribution, K^{*0} and ϕ peaks can be observed on top of a residual background [as an example, see Figs. 1 and 2, panels (b) and (d)]. The residual

background may be due to correlated πK or $K K$ pairs emitted within a jet, correlated pairs from particle decays (with three or more stable particles at the end of the decay chain), or misidentified correlated pairs (e.g., a $\rho \to \pi\pi$ decay being misidentified as a $K^{*0} \to \pi K$ decay). Differences in the structure of the two mixed events, including differences in the event planes, elliptic flow, primary vertices, and multiplicities, can also lead to an imperfect combinatorial background (if necessary, such differences can be reduced through the use of similarity criteria for the mixed events as described above). Figures 1 and 2 show invariant-mass distributions for the K^{*0} and ϕ mesons, respectively (two p_T intervals each). Integrated over the full transverse-momentum range and using the same centrality interval of 0–80% for both particles, the uncorrected K^{*0} (ϕ) yield is 27.4 (5.9) million, or 2.2 (0.47) per event, with a significance of 86 (146). For

TABLE I. Values of systematic uncertainties (%) averaged over all p_T and centrality intervals for the yield [$d^2N/(dp_T dy)$], mass, and width and averaged over all centrality intervals for dN/dy and $\langle p_T \rangle$. The descriptions in the first column give the type of systematic uncertainty (see also the discussion in the text). Combinatorial background: mixed-event normalization region (Sec. IV). Fitting region: region used to fit invariant-mass peaks (Sec. IV). Residual background shape: residual background fitting function (Sec. IV). Yield extraction: resonance yield extraction method (Sec. IV). Peak shape: see Sec. IV. Particle identification: dE/dx cuts to identify decay products (Sec. V). Tracking/track selection: see Sec. V. Material budget: see Sec. V. p_T extrapolation: p_T distribution fitting function used for extrapolation (Sec. VI A). Normalization: see Sec. VI A. The ϕ mass includes an additional 0.01% systematic uncertainty coming from the uncertainty in the simulated ϕ mass (Sec. VI B). "Total" gives the average over all centrality and p_T intervals of the total systematic uncertainty. A dash (–) indicates that a particular type of uncertainty is not relevant for the given quantity.

Type	$d^2N/(dp_T dy)$		dN/dy		$\langle p_T \rangle$		Mass		Width	
	K^{*0}	ϕ	K^{*0}	ϕ	K^{*0}	ϕ	K^{*0}	ϕ	K^{*0}	ϕ
Combinatorial background	2.2	0.4	1.0	0.4	0.01	0.3	0.1	0.0001	2.0	0.4
Fitting region	9.9	3.5	6.2	2.7	5.7	0.9	0.4	0.0023	18.2	4.4
Residual background shape	5.8	2.7	2.1	1.2	2.2	0.7	0.3	0.0025	15.7	3.9
Yield extraction	2.5	1.2	1.4	0.6	1.2	0.3	–	–	–	–
Peak shape	5.2	3.3	2.7	2.7	1.8	0.5	0.3	0.0007	10.0	7.8
Particle identification	2.7	6.2	1.2	2.3	1.1	2.1	0.3	0.0130	4.4	10.3
Tracking/track selection	10.0	10.0	10.0	10.0	–	–	0.4	0.0038	3.0	5.5
Material budget	1.0	1.0	1.0	1.0	–	–	0.2	0.0100	–	–
p_T extrapolation	–	–	1.2	2.1	2.1	1.2	–	–	–	–
Normalization	2.7	3.3	2.7	3.3	–	–	–	–	–	–
Total	17.3	14.0	12.2	11.9	7.2	3.1	0.7	0.0192	26.4	16.7

each p_T and centrality interval, the background-subtracted invariant-mass distributions are fitted by using a combined function to describe the residual background and the signal peak (the peak fitting functions are described below). The fitting regions are $0.77 < m_{\pi K} < 1.02$ GeV/c^2 for the K^{*0} and $1 < m_{KK} < 1.07$ GeV/c^2 for the ϕ. The boundaries of the fitting region are varied by 10–50 MeV/c^2 for K^{*0} and 5–30 MeV/c^2 for the ϕ. The variation in the yields does not increase if the fitting region boundaries are varied by larger amounts. Varying the boundaries of the fitting region produces average variations in the K^{*0} (ϕ) yield of 9.9% (3.5%), which are added to the systematic uncertainties ("Fitting region" in Table I). The systematic uncertainties also include variations due to the order of the residual background polynomial (first, second, or third order). Varying the residual background polynomial changes the K^{*0} (ϕ) yield by 5.8% (2.7%) on average ("Residual background shape" in Table I).

For each p_T and centrality interval, the K^{*0} mass and width are extracted from a relativistic p-wave Breit-Wigner function with a Boltzmann factor:

$$\frac{dN}{dm_{\pi K}} = \frac{C m_{\pi K} \Gamma M_0}{\left(m_{\pi K}^2 - M_0^2\right)^2 + M_0^2 \Gamma^2}$$
$$\times \left[\frac{m_{\pi K}}{\sqrt{m_{\pi K}^2 + p_T^2}} \exp\left(-\frac{\sqrt{m_{\pi K}^2 + p_T^2}}{T}\right) \right]. \quad (1)$$

Here, C is an overall scale factor and M_0 is the pole mass. The Boltzmann factor [in square brackets in Eq. (1)] is based on the assumption that in A-A collisions the K^{*0} resonance is predominantly produced through scattering (e.g., $\pi K \to K^{*0}$) in a thermalized medium rather than directly from string fragmentation. The factor accounts for

the phase-space population of the parent pions and kaons [36–39]. The temperature T is fixed to 160 MeV; this is approximately equal to the chemical freeze-out temperature, and varying this temperature by ± 30 MeV does not produce a significant change in the K^{*0} mass position. The parameter Γ in Eq. (1) is not constant, but depends on $m_{\pi K}$, the pole mass M_0, the resonance width Γ_0, and the vacuum masses of the charged pion and charged kaon (M_π and M_K, respectively):

$$\Gamma = \Gamma_0 \frac{M_0^4}{m_{\pi K}^4} \left[\frac{\left(m_{\pi K}^2 - M_\pi^2 - M_K^2\right)^2 - 4 M_\pi^2 M_K^2}{\left(M_0^2 - M_\pi^2 - M_K^2\right)^2 - 4 M_\pi^2 M_K^2} \right]^{3/2}. \quad (2)$$

The K^{*0} yield is determined by integrating the background-subtracted invariant-mass distribution over the range $0.77 < m_{\pi K} < 1.02$ GeV/c^2, removing the integral of the residual background fit over the same range, and correcting the result to account for the yield outside that range. For this purpose, the K^{*0} peak is fitted with a nonrelativistic Breit-Wigner function with the width fixed to the vacuum value, allowing the yield in the tails outside the range of integration to be calculated. This corresponds to $\sim$9% of the total K^{*0} yield. As an alternative, the K^{*0} yield is also found by integrating the peak fitting functions. The systematic uncertainties of the p_T-differential K^{*0} yield, the p_T-integrated yield dN/dy, and the mean transverse momentum $\langle p_T \rangle$ account for variations due to the two methods applied in extracting the yield. This variation is 2.5% for the p_T-differential K^{*0} yield ("Yield extraction" in Table I). The K^{*0} yield is also extracted from a relativistic Breit-Wigner function and a nonrelativistic Breit-Wigner function with a free width. Changes in the experimental results due to these different peak fitting functions are incorporated into the systematic uncertainties. The K^{*0} yield varies by 5.2% on
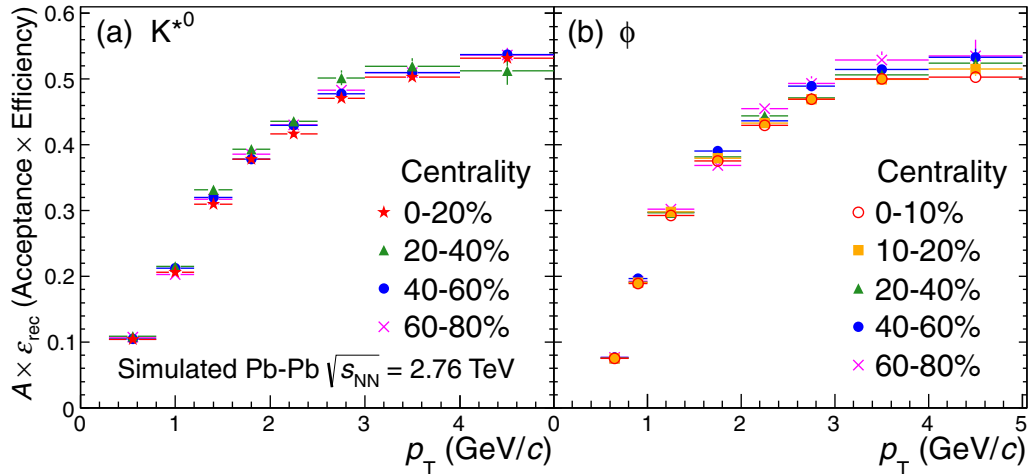
FIG. 3. (Color online) The product of the acceptance and the resonance reconstruction efficiency $A \times \varepsilon_{\mathrm{rec}}$ as a function of p_{T} for K^{*0} (a) and ϕ (b) mesons, calculated from simulated Pb-Pb collisions at $\sqrt{s_{NN}} = 2.76$ TeV. For the ϕ meson, only five examples for wide centrality intervals are shown. The acceptance A includes the effect of the resonance pair rapidity cut ($|y| < 0.5$). The values shown here do not include the branching ratios. Only statistical uncertainties are shown.

average when different peak fitting functions are used ("Peak shape" in Table I).

To find the ϕ mass and width for each p_{T} and centrality interval, the peak is fitted by using a Voigtian function.[2] This is the convolution of a nonrelativistic Breit-Wigner peak and a Gaussian, which accounts for the detector resolution:

$$\frac{dN}{dm_{KK}} = \frac{C\Gamma_0}{(2\pi)^{3/2}\sigma} \int_{-\infty}^{\infty} \left\{ \exp\left[-\frac{(m_{KK} - m')^2}{2\sigma^2} \right] \right.$$
$$\left. \times \frac{1}{(m' - M_0)^2 + \Gamma_0^2/4} dm' \right\}. \quad (3)$$

The mass resolution parameter σ, which has been shown to be independent of collision centrality, has been constrained to the value extracted from fits of simulated ϕ signal peaks. This value is about 1.2 MeV/c^2 for $p_{\mathrm{T}} \approx 0.6$ GeV/c. It reaches a minimum of about 1 MeV/c^2 for $p_{\mathrm{T}} \approx 1.2$ GeV/c and increases to about 1.5 MeV/c^2 for $p_{\mathrm{T}} = 4$–5 GeV/c. To estimate σ, the production and decay of ϕ mesons are simulated using HIJING [40], while the propagation of the decay products through the ALICE detector material is described using GEANT 3 [41]. The ϕ yield is determined through the same procedure used for the K^{*0}. The range of integration is $1.01 < m_{KK} < 1.03$ GeV/c^2. The yield in the tails is about $\sim$13% of the total ϕ yield, which is computed using the same Voigtian fits that are used to find the mass and width. Average variations in the ϕ yield of 1.2% are observed for the two different yield extraction methods. Different peak shapes are used in order to obtain alternate measurements of the yield,

---

[2]The choice of fitting functions for the two resonances is driven by the different widths. The K^{*0} has a width much larger than the resolution; therefore, a Voigtian fit is not necessary. However, since the K^{*0} is broad enough, its shape may be influenced by phase-space effects. The ϕ has a width of the same order of magnitude as the resolution and phase-space effects can be neglected.

mass, and width. The resolution σ is varied within the range of values observed in the simulation. Fits are also performed with the width fixed to the vacuum value while the resolution is kept as a free parameter. On average, the ϕ yield varies by 3.3% when different peak fitting functions are used.

V. YIELD CORRECTIONS

To obtain the corrected resonance yields, the raw yields are divided by the decay branching ratios [35], the acceptance A, the resonance reconstruction efficiency $\varepsilon_{\mathrm{rec}}$, and the particle identification (PID) efficiency $\varepsilon_{\mathrm{PID}}$. The acceptance accounts for the geometrical acceptance of the ALICE detector, the $|y| < 0.5$ resonance rapidity cut, and in-flight decays of the pions and kaons used to reconstruct the resonances. The PID efficiency accounts for the particle identification cuts used to identify the species of the decay-product candidates, i.e., the dE/dx cuts in the TPC. The factor $\varepsilon_{\mathrm{rec}}$ accounts for the remainder of the efficiency, including the tracking efficiency and the cuts used to select good-quality tracks coming from the primary vertex. The product $A \times \varepsilon_{\mathrm{rec}}$ is extracted from the same HIJING simulations that are used to estimate the mass resolution (with 9×10^5 generated K^{*0} and 4×10^5 generated ϕ mesons). The factor $A \times \varepsilon_{\mathrm{rec}}$ is the fraction of simulated resonances for which both decay products are reconstructed in the ALICE detector and pass the track selection cuts (PID cuts excluded). Figure 3 shows $A \times \varepsilon_{\mathrm{rec}}$ for K^{*0} and ϕ mesons as a function of p_{T} in different centrality intervals. The efficiency $\varepsilon_{\mathrm{PID}}$ is the product of the independent dE/dx-cut efficiencies for each decay product. The dE/dx distributions of the decay-product candidates are Gaussians with resolution σ_{TPC}. When PID cuts of $2\sigma_{\mathrm{TPC}}$ are applied to the dE/dx values of the pion and kaon candidates (i.e., for both resonance decay products) $\varepsilon_{\mathrm{PID}} = 91.1\%$. The use of different dE/dx cuts ($1.5\sigma_{\mathrm{TPC}}$ and $2.5\sigma_{\mathrm{TPC}}$) can result in large changes in the shape of the residual background, which affects the extracted resonance signal. The K^{*0} (ϕ) yield varies by 2.7% (6.2%) on average, and these

variations are incorporated into the systematic uncertainties (see "Particle identification" in Table I). A systematic uncertainty of 10% (for all p_T and centrality intervals), adapted from the analysis described in Ref. [42], accounts for variations in the yields due to the tracking efficiency and different choices of track quality cuts ("Tracking/track selection" in Table I). A systematic uncertainty of 1% (for all p_T and centrality intervals), which accounts for the uncertainty in the yield due to the uncertainty in the material budget of the ALICE detector ("Material budget" in Table I), is estimated based on [43]. The uncertainties in the branching ratios [35] are negligible in comparison to the total systematic uncertainties. The yields extracted with different cuts on the primary vertex z position are found to be consistent with each other.

VI. RESULTS AND DISCUSSION

A. Transverse-momentum distributions

The p_T distributions of the K^{*0} and ϕ mesons for $|y| < 0.5$, normalized to the number of events and corrected for the efficiency, acceptance, and branching ratio of the decay channel, are shown in Fig. 4. For central (peripheral) collisions the statistical uncertainty is approximately 3% (4%) near the maximum of the p_T distribution and increases to approximately 7% (10%) in the highest p_T bin; the systematic uncertainties are summarized in Table I. In order to extract the values of the mean transverse momentum $\langle p_T \rangle$ and the p_T-integrated particle yield dN/dy, these p_T distributions are fitted with a Boltzmann-Gibbs blast-wave function [44], which assumes that the emitted particles are locally thermalized in a uniform-density source at a kinetic freeze-out temperature $T_{\rm kin}$ and move with a common collective transverse radial flow velocity field. In this parametrization,

$$\frac{1}{p_T}\frac{dN}{dp_T} \propto \int_0^R r\,dr\,m_T\,I_0\left(\frac{p_T\sinh\rho}{T_{\rm kin}}\right)K_1\left(\frac{m_T\cosh\rho}{T_{\rm kin}}\right).$$

(4)

Here, the transverse mass $m_T = \sqrt{m^2 + p_T^2}$, I_0 and K_1 are modified Bessel functions, R is the fireball radius, and r is the radial distance in the transverse plane. The velocity profile ρ is

$$\rho = \tanh^{-1}\beta_T = \tanh^{-1}\left[\left(\frac{r}{R}\right)^n \beta_s\right],$$

(5)

where β_T is the average transverse expansion velocity and β_s is the transverse expansion velocity at the surface. The free parameters in the fits are $T_{\rm kin}$, β_s, and the velocity profile exponent n. These fits have $\chi^2/n_{\rm dof} < 1.3$ for all centrality intervals. Between central and peripheral collisions, it is observed that the temperature and the velocity profile exponent n increase, while the expansion velocity decreases, trends which are also observed in blast-wave fits of $\pi^\pm$, $K^\pm$, and (anti)proton p_T distributions in the same collision system [34]. The behavior of $T_{\rm kin}$ and β_s as a function of centrality is also observed at RHIC [45,46]. These trends are consistent with a scenario in which the fireballs created in peripheral collisions have shorter lifetimes than in central collisions, with higher freeze-out temperatures and less time to build up radial flow [47].
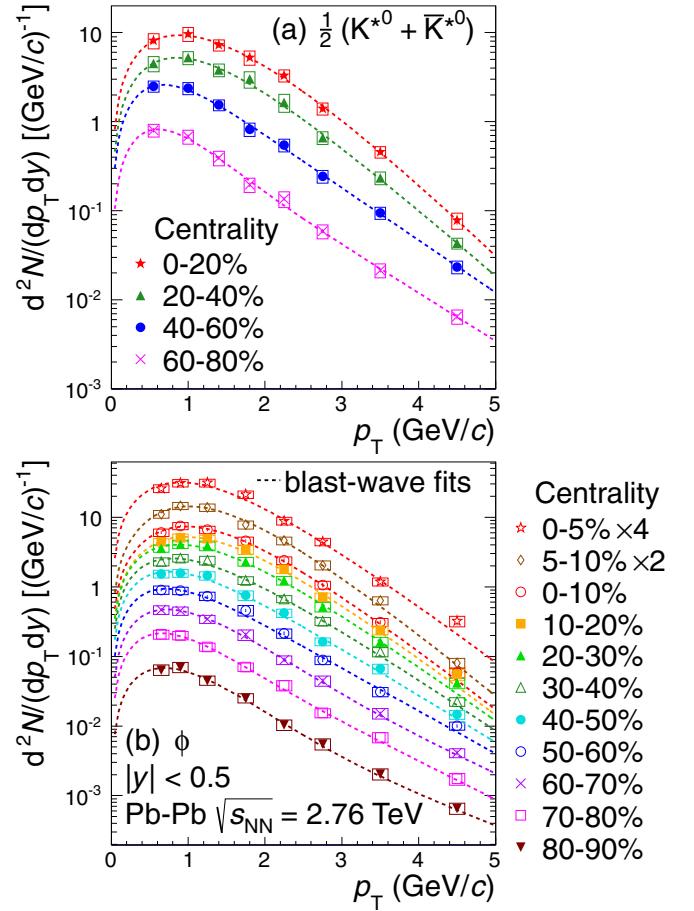

FIG. 4. (Color online) Transverse-momentum distributions of K^{*0} (a) and ϕ (b) mesons in multiple centrality intervals with blast-wave fitting functions. The data are the bin-averaged yields plotted at the bin centers. The statistical uncertainties are shown as bars and are frequently smaller than the symbol size. The total systematic uncertainties (including p_T-uncorrelated and p_T-correlated components) are shown as boxes.

In order to find dN/dy the measured resonance p_T distributions are integrated, while the fits are used to estimate the resonance yields at low and high p_T, where no signal could be measured. The low-p_T extrapolation region [$p_T(K^{*0}) < 0.3$ GeV/c and $p_T(\phi) < 0.5$ GeV/c] accounts for 5% (14%) of the total K^{*0} (ϕ) yield, while the high-p_T extrapolation region ($p_T > 5$ GeV/c) accounts for $\sim 0.1\%$ ($<0.5\%$) of the total yield. Alternate functions are also used to fit the resonance p_T distributions: Lévy-Tsallis functions [48,49] for both resonances as well as exponential functions in transverse mass for the calculation of dN/dy for ϕ. Variations in dN/dy and $\langle p_T \rangle$ due to the choice of the fitting function are incorporated into the systematic uncertainties ("p_T extrapolation" in Table I). The values of dN/dy for K^{*0} (ϕ) vary by 1.2% (2.1%) on average when the alternate fitting functions are used. Uncertainties in the boundaries of the centrality percentiles result in a normalization uncertainty for the particle yields. The values of the normalization uncertainty reported in Ref. [34] (ranging from 0.5% for central collisions
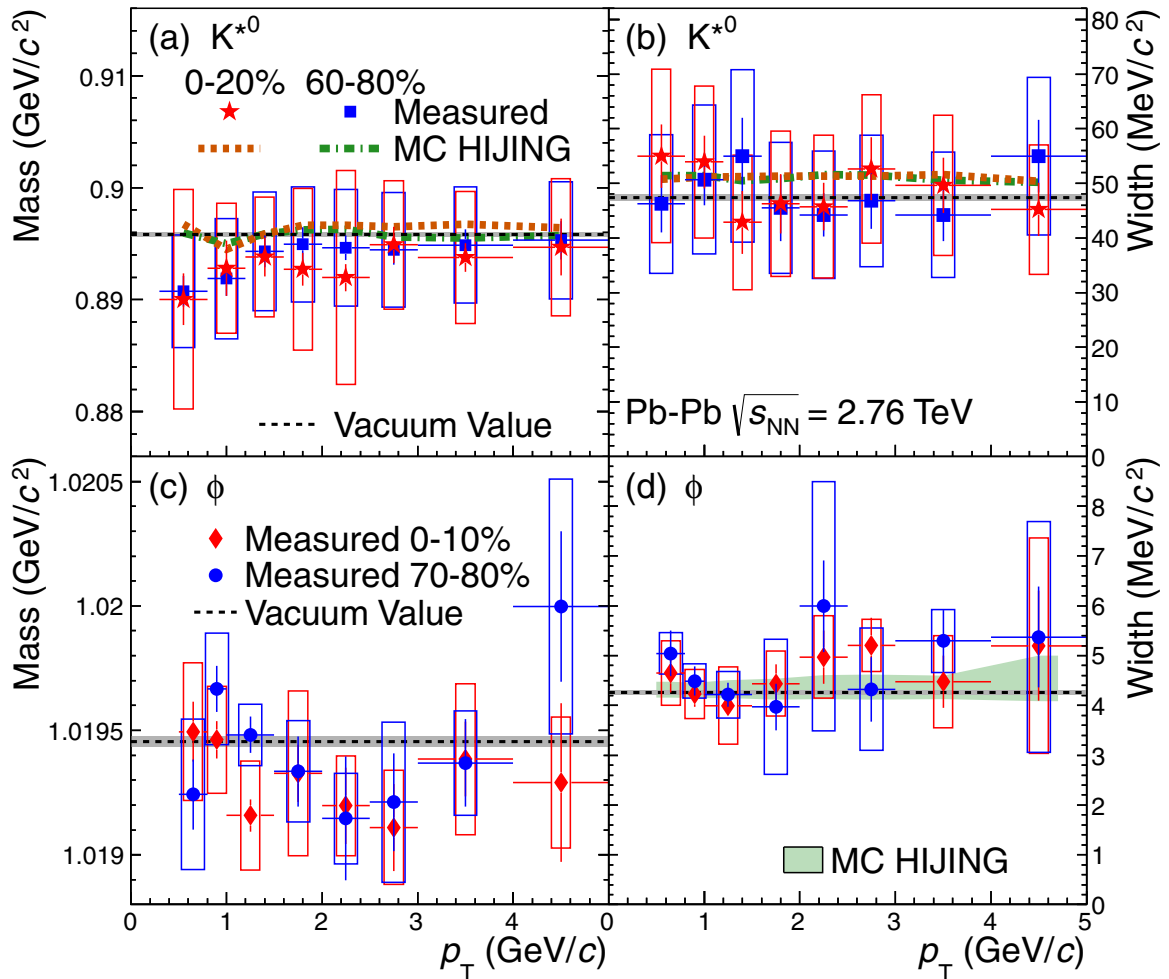
FIG. 5. (Color online) Measured K^{*0} meson mass (a) and width (b) in Pb-Pb collisions at $\sqrt{s_{NN}} = 2.76$ TeV in the 0–20% and 60–80% centrality intervals, along with the values extracted from Monte Carlo HIJING simulations. Measured ϕ meson mass (c) and width (d) in Pb-Pb collisions at $\sqrt{s_{NN}} = 2.76$ TeV in the 0–10% and 70–80% centrality intervals. The ϕ width extracted from HIJING simulations is also shown. The vacuum values of the K^{*0} and ϕ mass and width [35] are indicated by the horizontal dashed lines. The statistical uncertainties are shown as bars and the total systematic uncertainties (including p_T-uncorrelated and p_T-correlated components) are shown as boxes.

to $^{+12}_{-8.5}$% for peripheral collisions) are also used for K^{*0} and ϕ ("Normalization" in Table I).

B. Mass and width

The masses and widths of the K^{*0} and ϕ resonances [i.e., the fit parameters M_0 and Γ_0 from Eqs. (1)–(3)] are shown in Fig. 5 as a function of p_T for multiple centrality intervals. The systematic uncertainties in the masses and widths are evaluated as described in Secs. IV and V. In addition, variations in the masses and widths of the resonances due to changes in the track selection cuts (on DCA_{xy} and the number of TPC clusters) are incorporated into the systematic uncertainties (average values of 0.4% for the K^{*0} mass and 0.0038% for the ϕ mass). Uncertainties in the material budget of the ALICE detector introduce a further systematic uncertainty of approximately 0.2% (0.01%) in the K^{*0} (ϕ) mass. The measured K^{*0} mass has uncertainties of 5–10 MeV/c^2 (an uncertainty of approximately 4 MeV/c^2 is correlated between p_T bins) and is consistent with the mass values found in the HIJING simulation.

The measured K^{*0} width has uncertainties of 10–20 MeV/c^2 (2 MeV/c^2 correlated between p_T bins) and is also consistent with the values found in the simulation. The width of the ϕ meson is an order of magnitude smaller than the width of the K^{*0}. The ϕ mass is therefore measured with better precision than the K^{*0}, with systematic uncertainties of ~0.2 MeV/c^2. A mass shift, due to detector effects, is observed in the HIJING simulation. This shift ranges from -0.35 MeV/c^2 at low p_T to $+0.05$ MeV/c^2 at high p_T. The measured ϕ mass is corrected to account for this shift. The corrected ϕ mass, shown in Fig. 5(c), has uncertainties of 0.15–0.5 MeV/c^2 (0.1 MeV/c^2 correlated between p_T bins). The ϕ mass is observed to be consistent with the vacuum value. The ϕ width has uncertainties of 0.7–2 MeV/c^2 (0.3 MeV/c^2 correlated between p_T bins) and is consistent with the width observed in the HIJING simulation.[3]

---

[3]No centrality dependence is observed for the ϕ width in the simulation, so the average width for centrality 0–80% is plotted in Fig. 5(d).

TABLE II. The values of dN/dy, the K^{*0}/K^- and ϕ/K^- ratios, and $\langle p_T \rangle$ are presented for different centrality intervals. In each entry the first uncertainty is statistical. For dN/dy, the second uncertainty is the systematic uncertainty, not including the normalization uncertainty, and the third uncertainty is the normalization uncertainty. For K^{*0}/K^-, ϕ/K^-, and $\langle p_T \rangle$, the second uncertainty is the total systematic uncertainty. The ratios are calculated using K^- yields from [34].

		K^{*0}	
Centrality	dN/dy	K^{*0}/K^-	$\langle p_T \rangle$ (GeV/c)
0–20%	$16.6 \pm 0.6 \pm 2.5 \pm 0.1$	$0.20 \pm 0.01 \pm 0.03$	$1.31 \pm 0.04 \pm 0.11$
20–40%	$9.0 \pm 0.8 \pm 1.1 \pm 0.1$	$0.24 \pm 0.02 \pm 0.03$	$1.29 \pm 0.04 \pm 0.11$
40–60%	$3.9 \pm 0.3 \pm 0.4 \pm 0.1$	$0.28 \pm 0.02 \pm 0.03$	$1.16 \pm 0.04 \pm 0.08$
60–80%	$1.13 \pm 0.09 \pm 0.11 \pm 0.07$	$0.31 \pm 0.02 \pm 0.03$	$1.08 \pm 0.03 \pm 0.07$
		ϕ	
Centrality	dN/dy	ϕ/K^-	$\langle p_T \rangle$ (GeV/c)
0–5%	$13.8 \pm 0.5 \pm 1.7 \pm 0.1$	$0.127 \pm 0.004 \pm 0.014$	$1.31 \pm 0.04 \pm 0.06$
5–10%	$11.7 \pm 0.4 \pm 1.4 \pm 0.1$	$0.130 \pm 0.004 \pm 0.014$	$1.34 \pm 0.04 \pm 0.06$
10–20%	$9.0 \pm 0.2 \pm 1.0 \pm 0.1$	$0.134 \pm 0.003 \pm 0.013$	$1.34 \pm 0.03 \pm 0.04$
20–30%	$7.0 \pm 0.1 \pm 0.8 \pm 0.1$	$0.152 \pm 0.003 \pm 0.015$	$1.29 \pm 0.02 \pm 0.03$
30–40%	$4.28 \pm 0.09 \pm 0.48 \pm 0.09$	$0.144 \pm 0.003 \pm 0.014$	$1.25 \pm 0.03 \pm 0.03$
40–50%	$2.67 \pm 0.05 \pm 0.30 \pm 0.06$	$0.148 \pm 0.003 \pm 0.014$	$1.22 \pm 0.02 \pm 0.05$
50–60%	$1.49 \pm 0.03 \pm 0.16 \pm 0.05$	$0.145 \pm 0.003 \pm 0.014$	$1.20 \pm 0.02 \pm 0.04$
60–70%	$0.72 \pm 0.02 \pm 0.08 \pm 0.04$	$0.140 \pm 0.004 \pm 0.013$	$1.17 \pm 0.03 \pm 0.05$
70–80%	$0.30 \pm 0.01 \pm 0.04 \pm 0.02$	$0.133 \pm 0.005 \pm 0.015$	$1.12 \pm 0.03 \pm 0.03$
80–90%	$0.097 \pm 0.004 \pm 0.012^{+0.012}_{-0.008}$	$0.113 \pm 0.005 \pm 0.014$	$1.14 \pm 0.05 \pm 0.06$

Neither the mass nor the width of either resonance varies with centrality and no evidence is seen for a modification of the mass or width in Pb-Pb collisions at $\sqrt{s_{NN}} = 2.76$ TeV. The masses and widths of these resonances have also been studied at lower collision energies. No significant change in the mass or width of the K^{*0} meson is observed by the STAR Collaboration in Au-Au and Cu-Cu collisions at $\sqrt{s_{NN}} = 62.4$ GeV and $\sqrt{s_{NN}} = 200$ GeV [50]. The STAR Collaboration observes that the measured mass and width of the ϕ meson deviate from the values extracted from simulations at low p_T ($\lesssim 1.5$ GeV/c) in pp, d-Au, and Au-Au collisions at $\sqrt{s_{NN}} = 200$ GeV and Au-Au collisions at $\sqrt{s_{NN}} = 62.4$ GeV [51]. However, the deviations do not appear to depend on the size of the collision system and are likely due to detector effects that are not properly reproduced in the simulations. No clear evidence is observed for changes in the ϕ mass or width by the PHENIX Collaboration in Au-Au collisions at $\sqrt{s_{NN}} = 200$ GeV [46], nor by the NA49 Collaboration in Pb-Pb collisions at $\sqrt{s_{NN}} = 6$–17 GeV [52].

C. Particle ratios and interactions in the hadronic phase

Table II gives the values of dN/dy, the p_T-integrated particle yields for $|y| < 0.5$, for the K^{*0} and ϕ resonances in different centrality intervals. This table also includes the ratios of p_T-integrated particle yields K^{*0}/K^- and ϕ/K^-, which are calculated using the dN/dy values for K^- from [34]. These ratios are shown in Fig. 6 for Pb-Pb collisions at $\sqrt{s_{NN}} = 2.76$ TeV and pp collisions at $\sqrt{s} = 7$ TeV [54,55]. These ratios are presented as a function of $(dN_{\rm ch}/d\eta)^{1/3}$ (the cube root of the charged-particle multiplicity density measured at mid-rapidity) [31,53] for reasons discussed below. The K^{*0}/K^- ratio is observed to be lower in central Pb-Pb colli-

sions [larger values of $(dN_{\rm ch}/d\eta)^{1/3}$] than in pp and peripheral Pb-Pb collisions. When the K^{*0}/K^- ratio in central collisions is divided by the K^{*0}/K^- ratio in peripheral collisions the
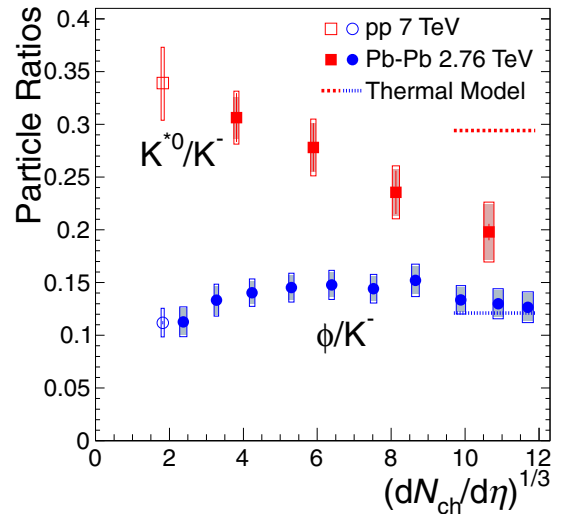

FIG. 6. (Color online) Ratios of p_T-integrated particle yields K^{*0}/K^- and ϕ/K^- as a function of $(dN_{\rm ch}/d\eta)^{1/3}$ [31,53] for Pb-Pb collisions at $\sqrt{s_{NN}} = 2.76$ TeV and pp collisions at $\sqrt{s} = 7$ TeV [54,55]. The values of $dN_{\rm ch}/d\eta$ were measured at mid-rapidity. The statistical uncertainties are shown as bars. The shaded boxes show systematic uncertainties that are not correlated between centrality intervals, while the open boxes show the total systematic uncertainties including both correlated and uncorrelated sources. The values given by a grand-canonical thermal model with a chemical freeze-out temperature of 156 MeV are also shown [56].

result[4] is 0.65 ± 0.11, which is different from unity at the 3.2σ level. On the other hand, the ϕ/K^- ratio does not depend strongly on collision centrality and may be enhanced in mid-central collisions with respect to peripheral and *pp* collisions. The value of the ϕ/K^- ratio in central Pb-Pb collisions is consistent with the value measured in *pp* collisions.

As discussed in Sec. I, it is possible that resonance yields are modified during the hadronic phase by rescattering (which would reduce the measured yields) and regeneration (which would increase the yields). The observed suppression of the K^{*0}/K^- ratio may be the result of these effects, with rescattering dominating over regeneration. The fact that the ϕ/K^- ratio does not exhibit suppression for central collisions suggests that the ϕ (which has a lifetime an order of magnitude larger than the K^{*0}) might decay predominantly outside the hadronic medium. Of K^{*0} mesons with momentum $p = 1$ GeV/c, 55% will decay within 5 fm/c of production (a typical estimate for the time between chemical and kinetic freeze-out in heavy-ion collisions [17,57]), while only 7% of ϕ mesons with $p = 1$ GeV/c will decay within that time. It should be noted that elastic scattering of the resonance decay products might be expected to broaden the measured K^{*0} invariant-mass distribution, which is not observed. The simultaneous observation of K^{*0}/K^- suppression but no K^{*0} width modification could be explained by decay-product rescattering if that process were to take place predominantly through elastic scattering with large momentum transfers (which would make the modified signal indistinguishable from the background) or through pseudoelastic scattering via other resonances.

In Fig. 6 the K^{*0}/K^- and ϕ/K^- ratios have been plotted as a function of $(dN_{\rm ch}/d\eta)^{1/3}$ in order to study whether the strength of the suppression might be related to the system radius. It is an established practice in femtoscopy studies to plot the HBT radii as a function of $(dN_{\rm ch}/d\eta)^{1/3}$ [58]. In some cases these radii have been observed to increase approximately linearly with $(dN_{\rm ch}/d\eta)^{1/3}$ [58,59], suggesting that $(dN_{\rm ch}/d\eta)^{1/3}$ might be used as a proxy for the system radius. If it is assumed that the suppression of the K^{*0} yield is due to rescattering and that the strength of rescattering effects is proportional to the distance which the decay products travel through the hadronic medium, the K^{*0}/K^- ratio would be expected to decrease as a decaying exponential in $(dN_{\rm ch}/d\eta)^{1/3}$. The observed dependence of the K^{*0}/K^- ratio on the multiplicity is consistent with the behavior that would be expected if rescattering were the cause of the suppression.

Figure 6 also includes the values given by a thermal model [56] for the K^{*0}/K^- and ϕ/K^- ratios in central Pb-Pb collisions at $\sqrt{s_{NN}} = 2.76$ TeV, with a chemical freeze-out temperature of 156 MeV and a baryochemical potential of 0 MeV. This thermal model does not include rescattering effects. These results were obtained by fitting a variety of particle yields measured in this collision system. The ϕ yield was included in the fit, but the K^{*0} was excluded due to the possibility that its yield could be modified as discussed above. The ϕ yield

from the fit agrees with the measured yield within 0.5 times the uncertainties and the fit results are not expected to change significantly if the ϕ is excluded. The K^{*0}/K^- ratio given by the thermal model is about 50% larger than the measured ratio. The thermal-model ϕ/K^- ratio for central Pb-Pb collisions at $\sqrt{s_{NN}} = 2.76$ TeV is consistent with the measured value.

The measured K^{*0}/K^- and ϕ/K^- ratios are compared in Fig. 7 to results for different collision systems and energies, plotted as a function of $(dN_{\rm ch}/d\eta)^{1/3}$ and $\sqrt{s_{NN}}$. This figure also includes the same thermal-model ratios for central Pb-Pb collisions shown in Fig. 6. The K^{*0}/K^- ratio is compared in Figs. 7(a) and 7(b) to results for different collision systems at RHIC[5] [36,50,60,69] and LHC [34,54,55] energies. The K^{*0}/K^- ratio is plotted as function of $(dN_{\rm ch}/d\eta)^{1/3}$ [31,53,68,69] in panel (a). In general, these values appear to follow a single trend independent of collision energy, tending to exhibit suppression in central *A-A* collisions with respect to *pp*, *d*-Au, and peripheral *A-A* collisions. The decrease in the K^{*0}/K^- ratio between *pp* and central *A-A* collisions is similar at both RHIC and LHC energies. Refs. [36,50] also suggest that the decrease in this ratio for collisions at $\sqrt{s_{NN}} = 200$ GeV may be due to rescattering of the K^{*0} decay products in the hadronic medium. The same ratio is shown in panel (b) as a function of $\sqrt{s_{NN}}$ for *pp* collisions, as well as central *A-A* and *d*-Au collisions. The K^{*0}/K^- ratio is higher in *pp* collisions than in central Au-Au and Pb-Pb collisions. The value of the K^{*0}/K^- ratio is larger in central Cu-Cu than in central Au-Au collisions, which is expected due to the smaller size of the Cu-Cu collision system.

The ϕ/K^- ratio is compared in Figs. 7(c) and 7(d) to results for different collision systems at SPS [52,62,63], RHIC [46,51,61,64–66], and LHC [43,54,55,67] energies. The ϕ/K^- ratio is plotted as a function of $(dN_{\rm ch}/d\eta)^{1/3}$ [31,53,68,69] in panel (c) for collisions at $\sqrt{s_{NN}} = 200$ GeV and LHC energies. The measured ϕ/K^- ratio for *A-A* collisions tends to be larger at $\sqrt{s_{NN}} = 200$ GeV than at $\sqrt{s_{NN}} = 2.76$ TeV for similar values of $(dN_{\rm ch}/d\eta)^{1/3}$; however, the values are consistent within their uncertainties. As observed at LHC energies, the ϕ/K^- ratio at $\sqrt{s_{NN}} = 200$ GeV does not exhibit a strong centrality dependence, though there are indications of a small enhancement (not beyond the uncertainties) for mid-central and central *A-A* collisions. The ϕ/K^- ratio is shown in panel (d) as a function of $\sqrt{s_{NN}}$ for *pp* collisions and for central *A-A* and *d*-Au collisions. The ϕ/K^- ratio is independent of collision energy and system from RHIC to LHC energies,[6] while at SPS energies the ratio measured in Pb-Pb collisions is a factor of 2 larger than the ratio in *pp* collisions.

---

[4]This calculation excludes the tracking/track selection and material budget systematic uncertainties, which are assumed to be correlated between centrality intervals.
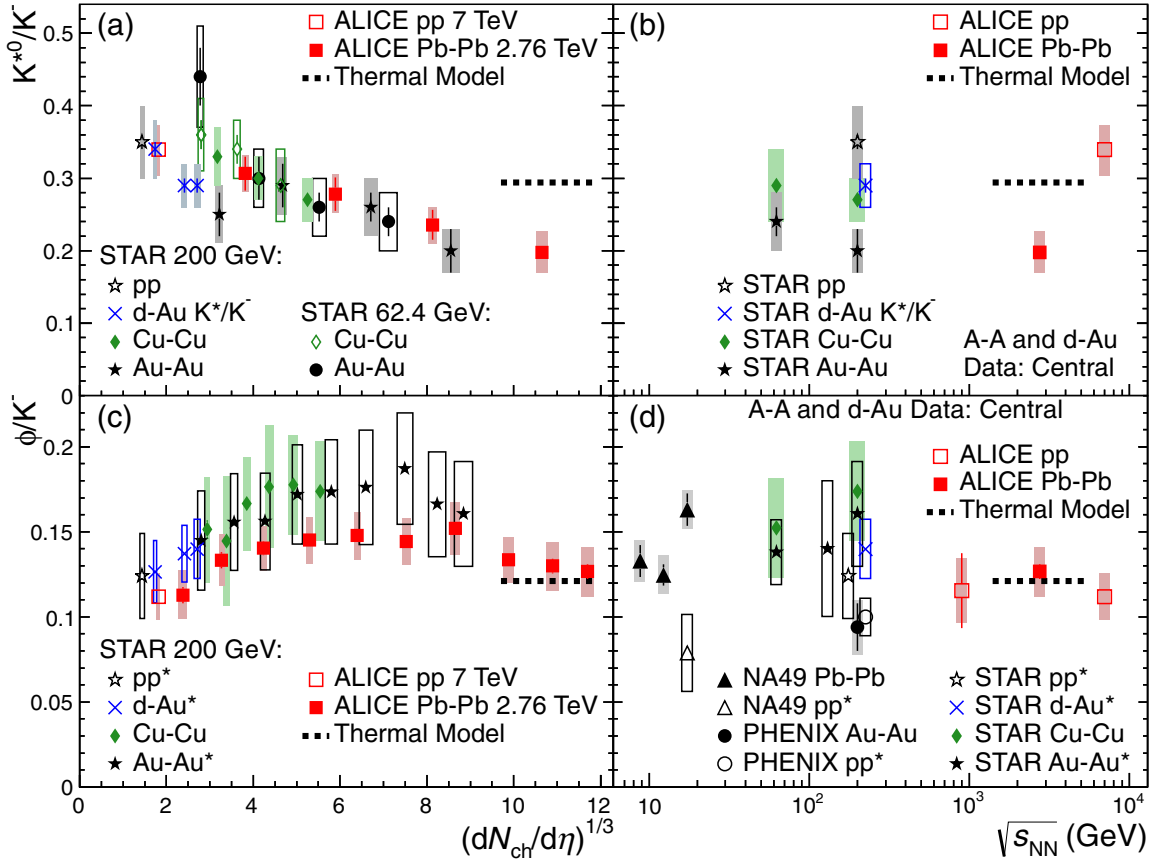
---

[5]For *d*-Au collisions [60] at $\sqrt{s_{NN}} = 200$ GeV the ratio K^*/K^- is plotted instead, where the yield in the numerator is calculated from a combination of all four $K^*(892)$ states.

[6]For Au-Au collisions at $\sqrt{s_{NN}} = 200$ GeV, the ϕ/K^- ratio measured by the PHENIX Collaboration [46] is ∼40% less than (and not consistent with) the ϕ/K^- ratio measured by the STAR Collaboration [51]. A possible explanation for this discrepancy is discussed in Ref. [7].

FIG. 7. (Color online) Particle ratios K^{*0}/K^- [panels (a) and (b)] and ϕ/K^- [panels (c) and (d)] in pp, d-Au, and A-A collisions [36,43,46,50–52,54,55,60–67]. In panels (a) and (c) these ratios are presented for different centrality intervals as a function of $(dN_{ch}/d\eta)^{1/3}$ [31,53,68,69]. The values of $dN_{ch}/d\eta$ were measured at mid-rapidity. In panels (b) and (d), these ratios are presented for pp, central d-Au, and central A-A collisions as a function of $\sqrt{s_{NN}}$. The values given by a grand-canonical thermal model with a chemical freeze-out temperature of 156 MeV are also shown [56]. For quantities marked "*", boxes represent the total uncertainty (separate uncertainties are not reported). Otherwise, bars represent the statistical uncertainties and boxes represent the systematic uncertainties (including centrality-uncorrelated and centrality-correlated components). For the d-Au data in panels (a) and (b), the numerator yield is derived from a combination of the charged and neutral $K^*(892)$ states. In panel (c), the two most central ϕ/K^- points for Au-Au collisions are for overlapping centrality intervals (0–5% and 0–10%). The following points have been shifted horizontally for visibility: the lowest-multiplicity d-Au points in panels (a) and (c), the d-Au points in panels (b) and (d), and the pp data points for $\sqrt{s_{NN}} = 200$ GeV in panel (d).

The measured p_T distributions and yields may reflect elastic and pseudoelastic interactions in the hadronic phase, with the magnitude of the change depending on the resonance lifetime. Thermal models, which give particle yields at chemical freeze-out, do not include these effects. Therefore, including the yields of short-lived resonances like K^{*0} in thermal-model fits might give misleading results. The model described in Refs. [15,22,23] is based on a thermal-model framework, but includes, in addition, rescattering effects which modify the resonance yields after chemical freeze-out. This model predicts particle ratios, including K^{*0}/K, as a function of the chemical freeze-out temperature and the lifetime of the hadronic phase. If an assumption is made about the value of the chemical freeze-out temperature, a measured K^{*0}/K ratio can be used to extract an estimate of the lifetime. Assuming a chemical freeze-out temperature of 156 MeV (based on thermal-model fits of ALICE data [56]) and using the measured K^{*0}/K^- ratio for the 0–20% centrality interval, it is possible to estimate a lower limit of 2 fm/c for the time between

chemical and kinetic freeze-out. Only a lower limit can be extracted because the model does not include regeneration of resonances in the hadronic medium. This limit on the hadronic lifetime is the same order of magnitude as the K^{*0} lifetime, but 23 times shorter than the ϕ lifetime. This value can be compared to the hadronic lifetime of >4 fm/c extracted using the same model and the $\Lambda(1520)/\Lambda$ ratio measured in Au-Au collisions at $\sqrt{s_{NN}} = 200$ GeV [70]. If a constant chemical freeze-out temperature is assumed, the increase in K^{*0}/K^- from central to peripheral Pb-Pb collisions (see Fig. 6) corresponds to a decreasing hadronic-phase lifetime and, equivalently, a larger kinetic freeze-out temperature. This is in qualitative agreement with results from blast-wave fits of particle p_T distributions [34], which also exhibit an increase in the kinetic freeze-out temperature for more peripheral collisions. Alternatively, if no hadronic lifetime or no rescattering is assumed, the model predicts a freeze-out temperature for the K^{*0} of about 120 ± 7 MeV.
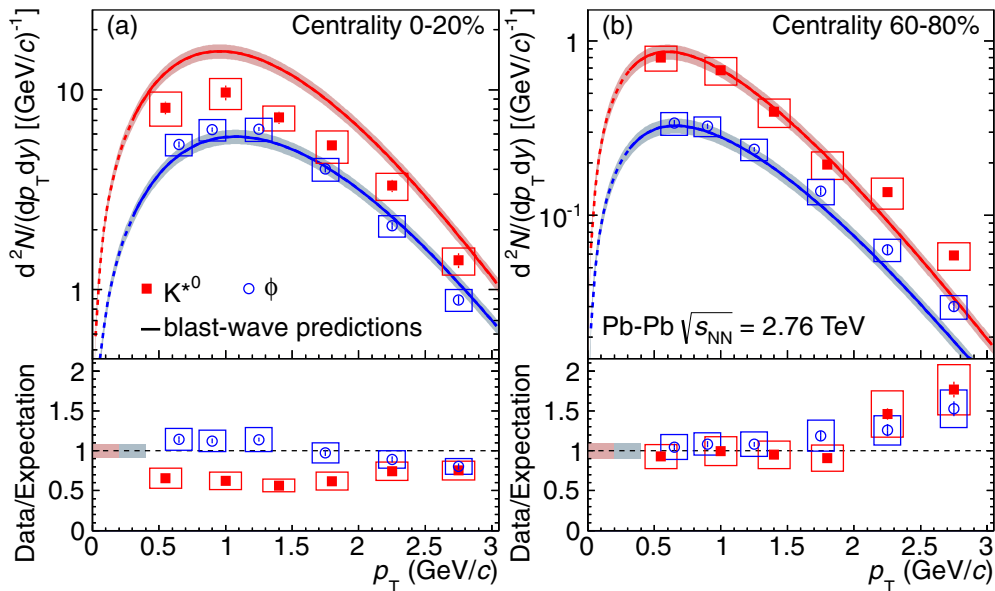
FIG. 8. (Color online) Transverse-momentum distributions of K^{*0} and ϕ resonances in Pb-Pb collisions at $\sqrt{s_{NN}} = 2.76$ TeV along with expected distributions for central (a) and peripheral (b) collisions. The shapes of the expected distributions are given by Boltzmann-Gibbs blast-wave functions [44] using parameters obtained from fits to $\pi^{\pm}$, $K^{\pm}$, and (anti)proton p_T distributions. The expected distributions are normalized so that their integrals are equal to the measured yield of charged kaons in Pb-Pb collisions [34] multiplied by the K^{*0}/K and ϕ/K ratios given by a thermal-model fit to ALICE data [56]. The lower panels show the ratios of the measured distributions to the values from the model. The statistical uncertainties are shown as bars and the systematic uncertainties from the measured p_T distributions (including p_T-uncorrelated and p_T-correlated components) are shown as boxes. The shaded bands (upper panels) and shaded boxes (lower panels) indicate the uncertainties in the normalization of the model distributions.

It should be noted that these estimates of the temperature or the lifetime of the hadronic phase are model dependent. The estimate of 2 fm/c for the lower limit of the lifetime of the hadronic phase is only valid insofar as the model described in Refs. [15,22,23] is valid. Later work by one of the same authors [8,9] uses a nonequilibrium thermal model to extract an estimate of 138 MeV for the freeze-out temperature with no time difference between chemical and kinetic freeze-out. However, this nonequilibrium model predicts a K^{*0}/K ratio that is essentially independent of centrality, which appears to disagree with the results reported above.

According to UrQMD [20,21] calculations for RHIC energies, the hadronic rescattering effect is expected to be momentum dependent, with greater strength for low-p_T resonances ($p_T \lesssim 2$ GeV/c) [14,17]. To investigate the p_T dependence of the observed suppression, the blast-wave model is used to generate expected transverse-momentum distributions without rescattering effects for the K^{*0} and ϕ resonances at kinetic freeze-out. The kinetic freeze-out temperature T_{kin}, velocity profile exponent n, and surface expansion velocity β_s (radial flow) are taken from simultaneous blast-wave fits of $\pi^{\pm}$, $K^{\pm}$, and (anti)proton p_T distributions in Pb-Pb collisions at $\sqrt{s_{NN}} = 2.76$ TeV [34]. For each centrality interval, these fits were performed over the ranges $0.5 < p_T < 1$ GeV/c for $\pi^{\pm}$, $0.2 < p_T < 1.5$ GeV/c for $K^{\pm}$, and $0.3 < p_T < 3$ GeV/c for (anti)protons. The simultaneous fits provide good descriptions of the particle p_T distributions within these fit ranges. The parameters used in the present study are the averages (weighted by the number of events multiplied by $dN_{\text{ch}}/d\eta$ [31]) of the values reported for the narrower centrality intervals in

Ref. [34]. For the 0–20% (60–80%) centrality interval, T_{kin} is 0.097 GeV (0.13 GeV), n is 0.73 (1.38), and β_s is 0.88 (0.80). For $p_T < 3$ GeV/c, these parameters are used with the blast-wave model to generate the shapes, but not the total yields, of expected p_T distributions for the K^{*0} and ϕ mesons. The expected K^{*0} (ϕ) distribution is normalized so that its integral is the $K^{\pm}$ yield dN/dy in Pb-Pb collisions [34] multiplied by the K^{*0}/K^- (ϕ/K^-) ratio given by a thermal-model fit to ALICE data [56] (with a chemical freeze-out temperature of 156 MeV). These are taken to be the expectations if hydrodynamics, as parameterized by the blast-wave model, describes the p_T distributions of the stable particles and the resonances simultaneously and if the K^{*0} and ϕ meson p_T distributions are not modified by any additional effects (e.g., rescattering or regeneration). The normalization depends on the parameters of the thermal model: if a temperature of 164 MeV [11] is used instead, the expected K^{*0} (ϕ) yield is 5% (6%) greater.

Figure 8 shows these expected K^{*0} and ϕ distributions (as solid lines), the measured resonance p_T distributions, and the ratios of the measurement to the model for central (0–20%) and peripheral (60–80%) collisions. The ratio of the measured ϕ meson p_T distribution to the expected distribution is around unity and no significant difference is observed in central collisions, nor in peripheral collisions for $p_T < 2$ GeV/c. On the other hand, the average measured/expected ratio for the K^{*0} is 0.6 ± 0.1 for $p_T < 3$ GeV/c in central collisions, a deviation from unity of about four times larger than the uncertainties. In peripheral collisions, the measured/expected ratio for the K^{*0} does not appear to deviate significantly from
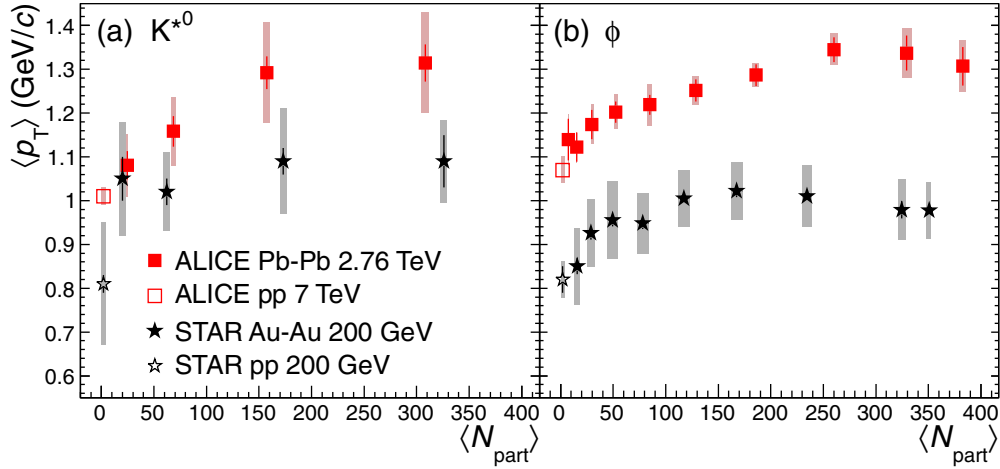
FIG. 9. (Color online) Mean transverse momentum $\langle p_T \rangle$ for K^{*0} (a) and ϕ mesons (b) as a function of $\langle N_{\text{part}} \rangle$ [32] in Pb-Pb collisions at $\sqrt{s_{NN}} = 2.76$ TeV. Also shown are measurements of $\langle p_T \rangle$ for minimum-bias pp collisions at $\sqrt{s} = 7$ TeV [54] and $\langle p_T \rangle$ for pp [36,61] and Au-Au [50,51,68] collisions at $\sqrt{s_{NN}} = 200$ GeV. Statistical uncertainties are shown as bars and systematic uncertainties are shown as boxes. The most peripheral K^{*0} points for A-A collisions (with $\langle N_{\text{part}} \rangle \approx 20$) have been shifted horizontally for visibility. The two most central ϕ points for Au-Au collisions are for overlapping centrality intervals (0–5% and 0–10%).

unity for $p_T < 2$ GeV/c. For central Pb-Pb collisions, the shape of the p_T distribution of K^{*0} for $p_T < 3$ GeV/c is consistent with the blast-wave parametrization of radial flow within uncertainties. Figure 8(a) shows a K^{*0} suppression of $\sim$40% in the measured low-p_T range and does not indicate the strongly momentum-dependent modification which is predicted by UrQMD for $p_T < 2$ GeV/c [14,17]. However, this UrQMD calculation counts the suppression relative to the sum of both primary as well regenerated K^{*0} resonances and therefore cannot be compared directly to the data.

The suggestion that K^{*0} suppression does not have a strong p_T dependence for $p_T < 3$ GeV/c might be interpreted as evidence that the reduction observed in the K^{*0} yield is not due to rescattering. However, it should be noted that regeneration is also expected to be more important at low p_T, which could counteract some of the low-p_T suppression that would be expected from rescattering alone. Furthermore, there is evidence for some increase in the measured/expected ratio for K^{*0} from $p_T = 1.2$ GeV/c to $p_T = 3$ GeV/c for central collisions. Further theoretical studies of the p_T dependence of K^{*0} suppression, with a full treatment of both rescattering and regeneration, would be helpful in determining the likelihood that rescattering is responsible for the observed decrease in the K^{*0} yield.

D. Mean transverse momentum

The mean transverse momentum $\langle p_T \rangle$ values for the K^{*0} and ϕ resonances are presented in Table II for different centrality intervals. Figure 9 shows $\langle p_T \rangle$ for the K^{*0} and ϕ resonances in Pb-Pb collisions at $\sqrt{s_{NN}} = 2.76$ TeV as a function of $\langle N_{\text{part}} \rangle$ [32]. Also shown are measurements of $\langle p_T \rangle$ in pp collisions at $\sqrt{s} = 7$ TeV [54] and in pp and Au-Au collisions at $\sqrt{s_{NN}} = 200$ GeV [36,50,51,61,68]. The values of $\langle p_T \rangle$ for the K^{*0} (ϕ) meson increase by about 20% (15%) in central Pb-Pb collisions relative to peripheral collisions. The values of $\langle p_T \rangle$ in pp collisions at $\sqrt{s} = 7$ TeV are consistent

with the values observed in peripheral Pb-Pb collisions at $\sqrt{s_{NN}} = 2.76$ TeV. For central collisions, $\langle p_T \rangle$ of the K^{*0} (ϕ) resonance measured in Pb-Pb collisions at $\sqrt{s_{NN}} = 2.76$ TeV is about 20% (30%) higher than the values measured in Au-Au collisions at $\sqrt{s_{NN}} = 200$ GeV. This is consistent with the observation [34] of increased radial flow in A-A collisions at the LHC relative to RHIC.

The values of $\langle p_T \rangle$ for π^+, K^+, K^{*0}, p, and ϕ in Pb-Pb collisions at $\sqrt{s_{NN}} = 2.76$ TeV are shown in Fig. 10 for different centrality intervals [32,34]. The values of $\langle p_T \rangle$ for the resonances in pp collisions at $\sqrt{s} = 7$ TeV are also shown
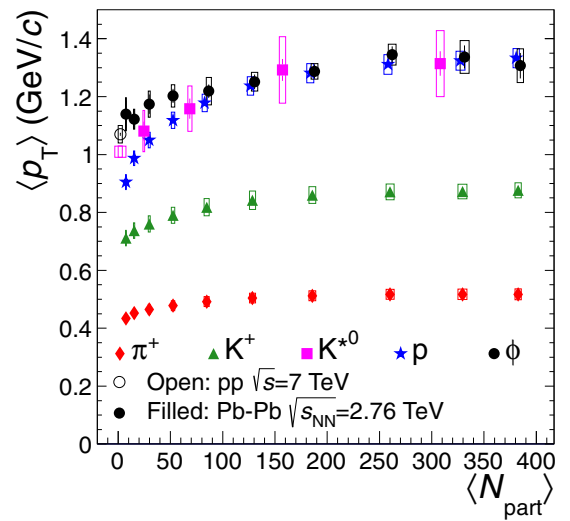
FIG. 10. (Color online) Mean transverse momentum of π^+, K^+, K^{*0}, p, and ϕ in Pb-Pb collisions at $\sqrt{s_{NN}} = 2.76$ TeV (filled symbols) [34] as a function of $\langle N_{\text{part}} \rangle$ [32]. Also shown are $\langle p_T \rangle$ values for the resonances in pp collisions at $\sqrt{s} = 7$ TeV [54] (open symbols). The measurements for central and mid-central ϕ and p have been shifted horizontally for visibility.

[54]. All particles exhibit an increase in $\langle p_T \rangle$ from peripheral to central Pb-Pb collisions, but this increase is greatest for the protons. While the increase in $\langle p_T \rangle$ from the most peripheral to most central measured interval is about 20% for π^+, K^+, K^{*0}, and ϕ, the value of $\langle p_T \rangle$ for protons increases by 50%. For the 0–40% most central collisions ($\langle N_{\mathrm{part}} \rangle \gtrsim 100$) the $\langle p_T \rangle$ values of the K^{*0}, proton, and ϕ all appear to follow the same trend. Within a given centrality interval, the $\langle p_T \rangle$ values of these three particles are consistent with each other within uncertainties. It should be noted that the masses of these three particles are similar: 896 MeV/c^2 for the K^{*0}, 938 MeV/c^2 for the p, and 1019 MeV/c^2 for the ϕ [35]. The similarity in $\langle p_T \rangle$ values is consistent with expectations from a hydrodynamic framework, in which p_T distributions would be determined predominantly by the particle masses. This is discussed further in the context of the p_T-dependent p/ϕ ratio in Sec. VI E 2.

E. Particle production

In this section, the p_T distributions and total yields of ϕ mesons are compared to theoretical models and other particle species (with different baryon number, mass, or strange quark content) to study particle production mechanisms. The ϕ meson is used for these studies because it lives long enough that its yields and p_T distributions do not appear to be affected by rescattering or regeneration in the hadronic phase. The possibility that such effects might change the K^{*0} p_T distributions and yields complicates any attempt to use that particle to study particle production. The predictions of hydrodynamic models, which have described the yields and p_T distributions of other hadrons with fair accuracy [34,71], are compared in Sec. VI E 1 to the p_T distribution of ϕ mesons in central Pb-Pb collisions. Differences in the production mechanisms of baryons and mesons can be studied through baryon-to-meson ratios. The p_T-dependent Ω/ϕ ratio, which compares baryons and mesons containing only strange (anti)quarks, is compared in Sec. VI E 1 to theoretical predictions and measurements in other collision systems. If hadron production can be explained in a hydrodynamic framework, the particle mass plays an important role in determining the shape of the p_T distribution. To study this aspect of particle production, in Sec. VI E 2 p_T distributions of ϕ mesons are compared to protons, which are baryons with a different quark content but a very similar mass to the ϕ. The dependence of particle production on the strange quark content is explored in Sec. VI E 3. Here the enhancement of the ϕ (which consists entirely of strange quarks but has no net strangeness) is compared to particles with 1, 2, and 3 units of open strangeness: the Λ, Ξ, and Ω baryons, respectively.

1. Comparisons to theoretical models

The measured ϕ meson p_T distribution for Pb-Pb collisions at $\sqrt{s_{NN}} = 2.76$ TeV (centrality 0–10%) is compared in Fig. 11 to five predicted distributions from hydrodynamic models. The measured and predicted distributions are shown in panel (a), while the ratio of the predicted distributions to the measured distribution is shown in panel (b). VISH2 + 1 is a (2 + 1)-dimensional viscous hydrodynamic model [73,74]. It has been
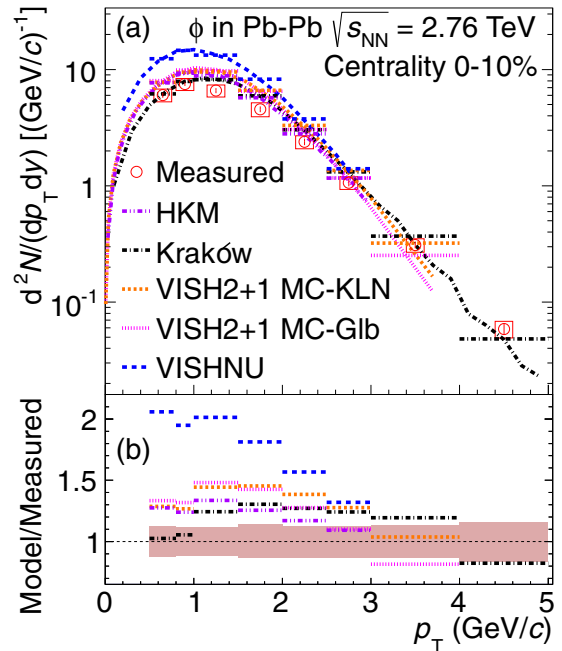
FIG. 11. (Color online) (a) Comparison of the measured ϕ meson p_T distribution in Pb-Pb collisions at $\sqrt{s_{NN}} = 2.76$ TeV (centrality 0–10%) to the distributions predicted by the Kraków model [72], two versions of the VISH2 + 1 model [73,74], the VISHNU [75,76] model, and the HKM [77,78]. The curves show the original predictions, while the horizontal lines show the predicted distributions rebinned so that they have compatible p_T bins with the measured distribution. (b) The ratio of the rebinned predictions to the measured distribution for ϕ mesons. The shaded band shows the fractional uncertainty of the measured data points.

observed to reproduce the total yields and the shapes of the p_T distributions of π and K within about 25% for $p_T < 2$ GeV/c in central Pb-Pb collisions [34]. VISH2 + 1 overestimates the total yields of the Ξ and Ω baryons, though it provides a fair description of the shape of the Ξ p_T distribution [71]. The VISH2 + 1 predictions shown in Fig. 11 are for two different sets of initial conditions: Monte Carlo Kharzeev-Levin-Nardi initial conditions (MC-KLN) with $\eta/s = 0.2$ [74] and Monte Carlo Glauber (MC-Glb) initial conditions with $\eta/s = 0.08$ [73]. These predictions are larger than the measured ϕ yield at low p_T. If the VISH2 + 1 MC-KLN prediction is fitted to the measured ϕ data through multiplication by a p_T-independent factor (0.74), it reproduces the shape of the measured p_T distribution for $p_T < 3$ with a χ^2 per degrees of freedom (χ^2/n_{dof}) value of 0.52 and no deviations beyond the experimental uncertainties. Similarly, the VISH2 + 1 MC-Glb prediction can be fitted to the measured ϕ p_T distribution, with a multiplicative constant of 0.74, $\chi^2/n_{\mathrm{dof}} = 1.1$, and no deviations beyond the experimental uncertainties.

The VISHNU model [75,76] is a hybrid model which connects the VISH2 + 1 hydrodynamic description of the QGP to a microscopic hadronic transport model (UrQMD) [20,21] to describe the hadronic phase. The VISNHU prediction for the ϕ yield is larger than the measured data, and does not appear to reproduce the shape of the p_T distribution (for

$p_T < 3$ GeV/c, $\chi^2/n_{\rm dof} = 2.6$ when the prediction is fitted to the data with a multiplicative constant of 0.53). It is also larger than either of the pure VISH2 + 1 predictions, which is attributed to the production of additional ϕ mesons in the hadronic phase through $K^- K^+$ scattering while ϕ decays are turned off [75].

The hydrokinetic model (HKM) [77,78] combines an ideal hydrodynamic phase with a hadronic cascade (UrQMD) after the hydrodynamic description of the partonic phase. Additional radial flow is built up during the hadronic phase and particle yields are affected by hadronic interactions (including baryon-antibaryon annihilation). HKM has been observed to reproduce the measured π, K, proton, Ξ and Ω data [34,71] better than VISH2 + 1, though it overestimates the yields of the multi-strange baryons. The ϕ yield is overestimated by HKM, though by a smaller amount than the VISH2 + 1 predictions. The HKM prediction can be fitted to the measured ϕ data through multiplication by a constant (0.80) for $p_T < 3$ GeV/c (its full range) with $\chi^2/n_{\rm dof} = 0.53$ and no deviations beyond the experimental uncertainties.

The Kraków model [72] is a hydrodynamic model which introduces a bulk viscosity in the transition from the partonic to the hadronic phase, producing deviations from local equilibrium within the fluid elements, thereby affecting the hadron p_T distributions and yields. This model reproduces the π, K, and (anti)proton p_T distributions within 20% for $p_T < 3$ GeV/c in central Pb-Pb collisions [34] and reproduces the Ξ p_T distributions within 30% in the same p_T range for the centrality range 0–60% [71]. It does not, however, describe the shape of the Ω p_T distribution. The Kraków model overpredicts the ϕ yield for $1 < p_T < 4$ GeV/c; however, it does not deviate from the measured yield by more than twice the uncertainty. The Kraków model prediction can be fitted to the measured ϕ meson p_T distribution through multiplication by a constant (0.85) for $p_T < 4$ GeV/c with $\chi^2/n_{\rm dof} = 1.1$ and no deviations beyond the uncertainties.

The hydrodynamic models considered above describe the measured ϕ meson p_T distribution with varying degrees of success. All of these models overpredict the ϕ yield, while all except the Kraków model predict softer p_T distributions for the ϕ meson than was measured. The best descriptions of the shape of the ϕ meson p_T distribution are given by the HKM and the Kraków model. Coupling hydrodynamics to a hadronic cascade, as is done in the KHM and VISHNU, has produced widely different results. For the ϕ, the two implementations of the VISH2 + 1 model produce similar results for $p_T < 2$ GeV/c, despite having different initial conditions and viscosities.

The ϕ and Ω are, respectively, a meson and a baryon made up entirely of strange (anti)quarks. In some particle production models, such as the HIJING/$B\overline{B}$ model [80,81], soft particles are produced through string fragmentation. The string tension is predicted [80] to influence the yields of strange particles, with multi-strange baryons and the Ω/ϕ ratio being particularly sensitive to the tension [82]. Figure 12 shows the $\Omega/\phi \equiv (\Omega^- + \overline{\Omega}^+)/\phi$ ratio as a function of p_T in Pb-Pb collisions at $\sqrt{s_{NN}} = 2.76$ TeV (centrality 0–10%) [71], pp collisions at $\sqrt{s} = 7$ TeV [54,79], and Au-Au collisions at
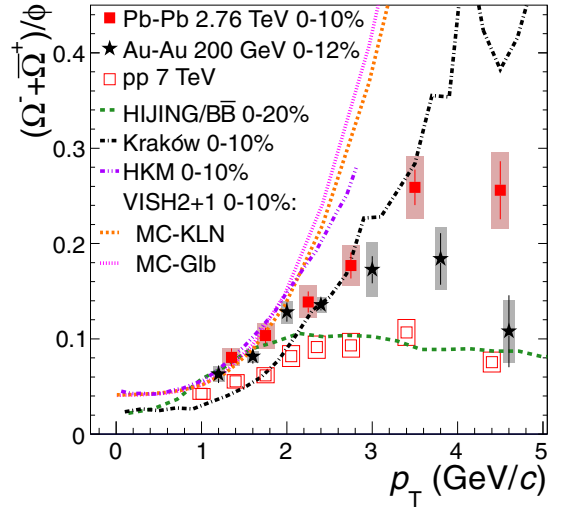
FIG. 12. (Color online) Ratio $(\Omega^- + \overline{\Omega}^+)/\phi$ as a function of p_T for Pb-Pb collisions at $\sqrt{s_{NN}} = 2.76$ TeV (centrality 0–10%) [71], pp collisions at $\sqrt{s} = 7$ TeV [54,79] and Au-Au collisions at $\sqrt{s_{NN}} = 200$ GeV (centrality 0–12%) [51]. The statistical uncertainties are shown as bars, systematic uncertainties (including p_T-uncorrelated and p_T-correlated components) are shown as shaded boxes, and the sum in quadrature of the statistical and systematic uncertainties (for the pp data) is shown as open boxes. Also shown are predictions of this ratio made by various models for central Pb-Pb collisions at $\sqrt{s_{NN}} = 2.76$ TeV (centrality 0–20% for HIJING/$B\overline{B}$, centrality 0–10% for the other models) [72–74,77,78,80,81].

$\sqrt{s_{NN}} = 200$ GeV (centrality 0–12%) [51]. The ratio measured in Pb-Pb collisions at $\sqrt{s_{NN}} = 2.76$ TeV is consistent with the ratio measured in Au-Au collisions at $\sqrt{s_{NN}} = 200$ GeV for $p_T \lesssim 3$ GeV/c, but is larger than the Au-Au measurement at high p_T. Predictions from the HIJING/$B\overline{B}$ and hydrodynamic models are also shown. None of these models is able to predict the measured Ω/ϕ ratio. HKM provides a better description of the Ω p_T distributions than VISH2 + 1; however, it overestimates the total yield [71]. The VISH2 + 1 and HKM predictions are consistent with the measured Ω/ϕ ratio for $p_T < 2$ GeV/c, but increase faster with p_T than the data for $p_T > 2$ GeV/c. The HKM does appear to provide a better description of the slope of the measured Ω/ϕ ratio. The Kraków model [72] underpredicts the measured data at low p_T, but is consistent with the data for $2 < p_T < 3.5$ GeV/c. This model is able to reproduce the measured Ω yield within about 30% [71], but does not reproduce the shape of the p_T distribution. The Ω/ϕ ratio predicted by the HIJING/$B\overline{B}$ v2.0 model [80,81,83,84], with a strong color field and a string tension of $\kappa = 1.8$ GeV/fm, reproduces neither the shape nor the values of the measured data. A larger string tension of $\kappa = 5.1$ GeV/fm gives a predicted Ω/ϕ ratio (not shown) that is at least a factor of three larger than the measured ratio. The same model can reproduce the Ω/ϕ ratio observed in pp collisions at $\sqrt{s} = 7$ TeV [54,79][7] with a string tension of $\kappa = 2$ GeV/fm, and describes the Ω/ϕ ratio observed in

---

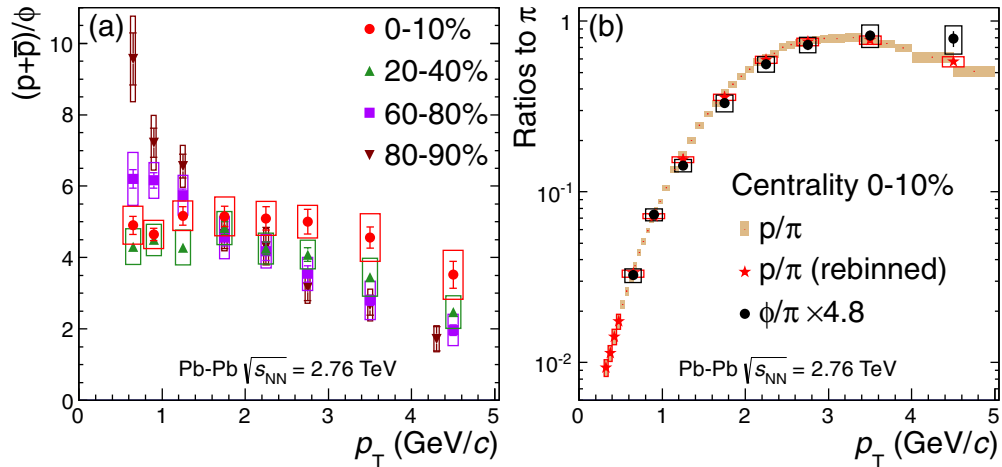[7]The prediction was calculated for $\sqrt{s} = 5$ TeV.

FIG. 13. (Color online) (a) Ratio p/ϕ as a function of p_T for Pb-Pb collisions at $\sqrt{s_{NN}} = 2.76$ TeV [34,86] for four centrality intervals. (b) Ratios of p and ϕ yields to charged pions as a function of p_T for central Pb-Pb collisions at $\sqrt{s_{NN}} = 2.76$ TeV [34,86]. The p/π ratio is presented using two p_T binning schemes: the ratio with its original measured bins is shown along with a recalculated version that uses the same bins as the ϕ meson p_T distribution for $0.5 < p_T < 5$ GeV/c. In order to show the similarity of the shapes of the two ratios for $p_T < 3$ GeV/c, the ϕ/π ratio has been scaled so that the ϕ and proton integrated yields are identical. In both panels, the statistical uncertainties are shown as bars and the total systematic uncertainties (including p_T-uncorrelated and p_T-correlated components) are shown as boxes.

Au-Au collisions at $\sqrt{s_{NN}} = 200$ GeV [82,85] with a string tension of $\kappa = 3$ GeV/fm.

2. Particles with similar masses

The proton and ϕ have similar masses, but different baryon numbers and quark content. If production of these particles is described within a hydrodynamic framework, the p_T distributions of these species are expected to have similar shapes, despite their different quantum numbers. Figure 13(a) shows the ratio $p/\phi \equiv (p + \bar{p})/\phi$ as a function of p_T for Pb-Pb collisions at $\sqrt{s_{NN}} = 2.76$ TeV [34,86] for different centralities.[8] For central collisions, the p/ϕ ratio is flat over the entire measured range. However, for noncentral collisions, this ratio is observed to decrease with p_T. This behavior can also be seen in the $\langle p_T \rangle$ values of p and ϕ in Fig. 10: these values are consistent with each other in central collisions, but $\langle p_T \rangle$ is lower for p than for ϕ in peripheral collisions. The flat p/ϕ ratio in central collisions indicates that, at LHC energies, the shapes of the p_T distributions of the p and ϕ at low and intermediate p_T are determined by the particle masses. One possible explanation for the nonconstant p/ϕ ratio in peripheral Pb-Pb collisions would be that the particles have a production mechanism in which the quark content is an important factor in determining the shapes of the p_T distributions. At RHIC energies, a splitting in the nuclear modification factor R_{CP} (the ratio of central to peripheral particle yields scaled by the number of binary collisions in the two centrality intervals), with baryons being less suppressed than mesons at intermediate p_T [36,87–90], has been taken as

evidence in favor of recombination models [91]. However, at LHC energies, the flat p/ϕ ratio suggests that recombination might not be suited to explain the shapes of the observed particle p_T distributions in central A-A collisions at low and intermediate p_T.

The $p/\pi \equiv (p + \bar{p})/(\pi^- + \pi^+)$ ratio [34,86] is shown in Fig. 13(b). When this ratio was first reported [34], it was not clear if the observed increase in p/π with transverse momentum is due to hydrodynamic effects or quark recombination. As shown in Fig. 13, the baryon-to-meson ratio p/π has a very similar shape to the meson-to-meson ratio $\phi/\pi \equiv \phi/(\pi^- + \pi^+)$ for $p_T < 3$ GeV/c. This indicates that the number of quarks is not the main factor that determines the shapes of particle p_T distributions at low and intermediate p_T in central collisions. This is contrary to the expectations from recombination, but consistent with hydrodynamic models.

3. Strangeness content

The enhancement ratio is defined as the yield (dN/dy) of a particle in A-A collisions normalized to $\langle N_{\text{part}} \rangle$ and divided by the same quantity in pp collisions[9] at the same energy. This ratio has been the traditional way of presenting strangeness production in heavy-ion collisions [71,90,92–99]. However, given the fact that charged-particle production increases in a nonlinear way with the number of participants [31], part of the enhancement observed using this ratio cannot be attributed to strangeness. A way to avoid this bias is to normalize to the pion yield. In order to allow for an easy comparison to previous measurements both approaches are discussed in this section.

---

[8]The values of the p/ϕ ratio for the 10–20% and 40–60% centrality intervals, which are not shown here, are available in the Durham Reaction Database.

[9]Reference yields measured in p-Be collisions have also been used [92,93].
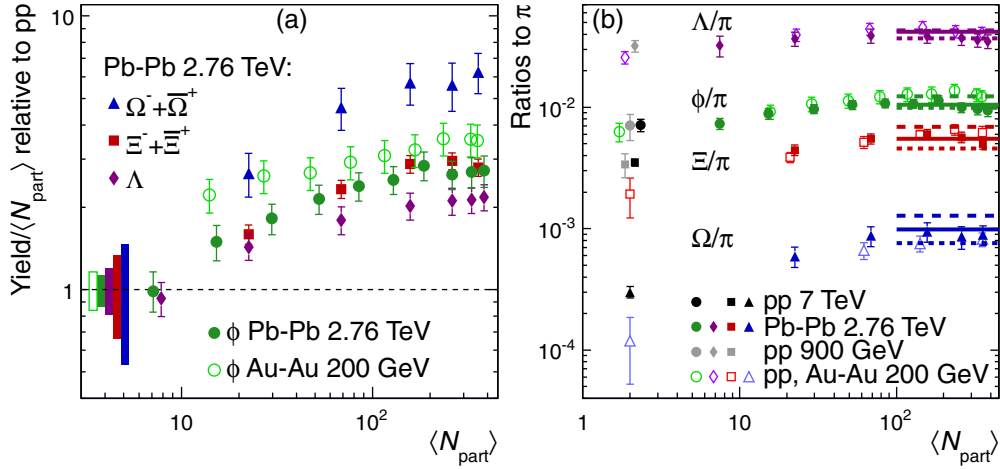
FIG. 14. (Color online) (a) Enhancement of ϕ, Λ, Ξ, and Ω in Pb-Pb collisions at $\sqrt{s_{NN}} = 2.76$ TeV [71,101], calculated using pp reference yields (extrapolated for Λ, interpolated for ϕ, Ξ, and Ω). Also shown is the enhancement of the ϕ in Au-Au collisions at $\sqrt{s_{NN}} = 200$ GeV [103], calculated using a measured pp reference yield. The enhancement value reported here is the ratio of the yield (dN/dy) of a particle in A-A collisions to the yield of that particle in pp collisions at the same energy, with both the numerator and denominator normalized by $\langle N_{\text{part}} \rangle$. The two most central ϕ enhancement values for Au-Au collisions are for overlapping centrality intervals (0–5% and 0–10%). Bars represent the uncertainties in the A-A yields (including centrality-uncorrelated and centrality-correlated components), while the boxes at low values of $\langle N_{\text{part}} \rangle$ represent the uncertainties of the pp reference yields. The ϕ and Λ measurements at $\langle N_{\text{part}} \rangle = 7.5$ have been shifted horizontally for visibility. (b) Ratios of particle yields to charged pion yields for Pb-Pb collisions at $\sqrt{s_{NN}} = 2.76$ TeV [34,71,101], Au-Au collisions at $\sqrt{s_{NN}} = 200$ GeV [51,68,90,104], and pp collisions at $\sqrt{s} = 200$ GeV [49,61,68], 900 GeV [43,67], and 7 TeV [54,55,79]. The lines show ratios given by grand-canonical thermal models with temperatures of 170 MeV [6] (upper dashed lines), 164 MeV [10] (solid lines), and 156 MeV [56] (lower dashed lines). The total uncertainties (including centrality-uncorrelated and centrality-correlated components) are shown as bars. Some of the measurements at $\langle N_{\text{part}} \rangle = 2$ have been shifted horizontally for visibility. The two most central ϕ/π values for Au-Au collisions are for overlapping centrality intervals (0–5% and 0–10%).

The ϕ yield in pp collisions at $\sqrt{s} = 2.76$ TeV has been estimated by interpolating between the measured yields at $\sqrt{s} = 900$ GeV [43] and $\sqrt{s} = 7$ TeV [54], assuming that the yield varies as s^n. Given the measured ϕ yields at $\sqrt{s} = 900$ GeV and $\sqrt{s} = 7$ TeV, the value of the power n was found to be 0.10. For comparison, the calculation of the enhancement values of multi-strange baryons at $\sqrt{s_{NN}} = 2.76$ TeV uses an energy dependence of $s^{0.13}$ to find the interpolated pp reference values [71]. The charged-particle pseudorapidity density is observed to vary as $s^{0.11}$ [100]. The systematic uncertainty in the interpolated ϕ yield is estimated by successively increasing, then decreasing each of the two measured points by its own uncertainty and repeating the interpolation procedure. The resulting variations in the interpolated yield are incorporated into the systematic uncertainty. The systematic uncertainty in the interpolated ϕ reference yield is 13%. Including the ϕ meson yields measured in pp collisions at $\sqrt{s} = 200$ GeV [61,65] in the interpolation does not significantly alter the result. The Λ enhancement in Pb-Pb collisions at $\sqrt{s_{NN}} = 2.76$ TeV, calculated using the yields reported in Ref. [101], is also reported below for the purpose of comparison with the ϕ. The reference Λ yield in pp collisions at $\sqrt{s} = 2.76$ TeV is estimated by extrapolating from the measured yield in (inelastic) pp collisions at $\sqrt{s} = 900$ GeV [43], assuming the same energy dependence as $dN_{\text{ch}}/d\eta$. The systematic uncertainty in this extrapolation is estimated by using the energy dependence

of the $\Lambda + \bar{\Lambda}$ yield in non-single-diffractive pp collisions at $\sqrt{s} = 200$ GeV, 900 GeV, and 7 TeV [49,102]. The uncertainty in the extrapolated Λ reference yield is 19%.

The enhancement values for ϕ for different centrality intervals are shown in Fig. 14(a) along with the enhancement values for Λ, Ξ, and Ω [71,101]. Enhancement values for ϕ in Au-Au collisions at $\sqrt{s_{NN}} = 200$ GeV [103] are also shown. The ϕ enhancement ratio decreases from $\sqrt{s_{NN}} = 200$ GeV to $\sqrt{s_{NN}} = 2.76$ TeV, a trend that has been observed for the other particles as well [71,99]. The values of the ϕ and Λ enhancement for the 80–90% centrality interval ($\langle N_{\text{part}} \rangle = 7.5$) are consistent with unity, i.e., the yields per participant nucleon of these particles in peripheral Pb-Pb collisions are consistent with the estimated yields in pp collisions. The yields of ϕ, Λ, Ξ, and Ω at LHC energies increase faster than linearly with $\langle N_{\text{part}} \rangle$ until $\langle N_{\text{part}} \rangle \approx 100$, while the enhancement values seem to be saturated for higher values of $\langle N_{\text{part}} \rangle$. The enhancement values increase with the number of strange valence (anti)quarks, a trend which is also observed at lower energies. For collisions at $\sqrt{s_{NN}} = 2.76$ TeV, the ϕ enhancement is consistent with the enhancement values of Λ (one strange valence quark), as well as Ξ^- and $\bar{\Xi}^+$ (two strange valence quarks or antiquarks). The central values of the ϕ enhancement tend to be between the Λ and Ξ enhancement values. A similar behavior is observed when the ϕ is compared to Λ, $\bar{\Lambda}$, and $\bar{\Xi}^+$ in Au-Au collisions at $\sqrt{s_{NN}} = 200$ GeV [99,103].

As an alternative to the standard $\langle N_{\mathrm{part}}\rangle$-based enhancement ratio discussed above, the yields of particles containing strange quarks are compared to pion yields. This is shown in Fig. 14(b) for A-A and pp collisions at RHIC and LHC energies [34,43,49,51,54,55,61,67,68,71,79,90,101]. The ratios shown are $\phi/\pi \equiv \phi/(\pi^- + \pi^+)$, $\Xi/\pi \equiv (\Xi^- + \overline{\Xi}^+)/(\pi^- + \pi^+)$, and $\Omega/\pi \equiv (\Omega^- + \overline{\Omega}^+)/(\pi^- + \pi^+)$. For Pb-Pb collisions at $\sqrt{s_{NN}} = 2.76$ TeV, $\Lambda/\pi \equiv 2\Lambda/(\pi^- + \pi^+)$, but otherwise $\Lambda/\pi \equiv (\Lambda + \overline{\Lambda})/(\pi^- + \pi^+)$. While the Λ/π, Ξ/π, and Ω/π ratios in pp collisions are higher at LHC energies than at RHIC energies, the ϕ/π ratio in pp collisions does not exhibit a significant change from $\sqrt{s} = 200$ GeV to 7 TeV. Relative to pp collisions, strangeness production in Pb-Pb collisions at $\sqrt{s_{NN}} = 2.76$ TeV at first increases with centrality and appears to saturate for $\langle N_{\mathrm{part}}\rangle \gtrsim 100$. A decrease in the ϕ/π, Λ/π, and Ξ/π ratios for the 0–20% most central collisions ($\langle N_{\mathrm{part}}\rangle \gtrsim 230$) may be present; however, the trend is flat within systematic uncertainties. The increase in these ratios from pp to central Pb-Pb collisions at LHC energies is ~3.3 for Ω/π, ~1.6 for Ξ/π, ~1.2 for Λ/π, and ~1.4 for ϕ/π. These values are about one half of the enhancement ratios discussed above. The fractional increase in the ϕ/π ratio is similar to the increases observed in both the Λ/π and Ξ/π ratios, a trend which is also observed in the standard enhancement ratios presented in the previous paragraph. At SPS energies, a study of the ϕ/π, K/π, and $(K/\pi)^2$ ratios suggests that the ϕ behaves as a particle with an effective strangeness quantum number between 1 and 2 [105]. The values of the ϕ/π, Λ/π, Ξ/π, and Ω/π ratios obtained from grand-canonical thermal models with temperatures of 170 MeV [6] (upper dashed lines), 164 MeV [10] (solid lines), and 156 MeV [56] (lower dashed lines) are also shown. It should be noted that the model using a temperature of 164 MeV gives a p/π ratio that is about 50% greater than the measured value.

VII. CONCLUSIONS

The p_{T} distributions, masses, and widths of K^{*0} and ϕ mesons have been measured at mid-rapidity ($|y| < 0.5$) in Pb-Pb collisions at $\sqrt{s_{NN}} = 2.76$ TeV using the ALICE detector. The masses and widths of these resonances, reconstructed via their hadronic decays, are consistent with the vacuum values. The measured $\langle p_{\mathrm{T}}\rangle$ is 15–20% higher in central Pb-Pb collisions than in peripheral collisions and it is found to be higher in A-A collisions at LHC energies than at RHIC energies. This suggests stronger radial flow at the LHC, which has also been concluded based on previous measurements of pion, kaon, and proton p_{T} distributions. Relative to the yields of charged kaons, the total yield (dN/dy) of K^{*0} is observed to be suppressed in central Pb-Pb collisions. When plotted as a function of $(dN_{\mathrm{ch}}/d\eta)^{1/3}$, the K^{*0}/K^- ratio appears to follow a single trend for both RHIC and LHC energies and for different collision systems. In contrast, no suppression is observed for the ϕ. When the p_{T} distributions of the K^{*0} and ϕ mesons are compared to expected distributions based on the blast-wave model (using parameters taken from fits to other

hadrons), K^{*0} suppression is observed in central collisions for transverse momenta $p_{\mathrm{T}} < 3$ GeV/c. The suppression of the integrated K^{*0} yield might be taken to suggest that rescattering of resonance decay products in the hadronic phase reduces the measurable yield of K^{*0} mesons. However, it is unclear if such a scenario can fully explain the observed p_{T} dependence of the K^{*0} suppression or the absence of broadening in its invariant-mass distribution. The lack of suppression for the ϕ meson could indicate that this particle decays outside the fireball due to its longer lifetime. The measured K^{*0}/K^- ratio is compared to an extended thermal-model prediction [15,22,23] that includes rescattering effects. By assuming a chemical freeze-out temperature of 156 MeV, a model-dependent estimate of 2 fm/c as the lower limit of the time between the chemical and kinetic freeze-out is extracted. The measurement of at least one more resonance-to-stable ratio [such as $\Lambda(1520)/\Lambda$] will allow both the lifetime of the hadronic phase and the chemical freeze-out temperature to be estimated simultaneously within the framework of this model. At LHC energies the ϕ, which has hidden strangeness, is enhanced by an amount similar to particles with one or two units of open strangeness. While a hydrodynamic framework can roughly describe the measured particle p_{T} distributions in Pb-Pb collisions at $\sqrt{s_{NN}} = 2.76$ TeV, inconsistencies nevertheless remain. For central collisions the p/ϕ ratio is flat as a function of transverse momentum for $p_{\mathrm{T}} \lesssim 3$ GeV/c. This is consistent with hydrodynamic models, thereby suggesting that mass and hence radial flow plays a dominant role in the determination of the shapes of p_{T} distributions at low and intermediate p_{T}. Models based on hydrodynamics (Kraków, HKM, and VISH2 + 1) are able to reproduce the shape of the ϕ meson p_{T} distribution fairly well, but overestimate the ϕ yield. These models describe the p_{T} distributions of other particles, such as π, K, and protons, reasonably well, but they encounter difficulties in describing the p_{T} distribution of the Ω and the Ω/ϕ ratio.

[1] P. Petreczky, Review of recent highlights in lattice calculations at finite temperature and finite density, PoS(Confinement X) 028 (2012).

[2] S. Borsányi, G. Endrődi, Z. Fodor, A. Jakovác, S. D. Katz, S. Krieg, C. Ratti, and K. K. Szabó, The QCD equation of state with dynamical quarks, J. High Energy Phys. 11 (2010) 077.

[3] S. Borsányi, Z. Fodor, C. Hoelbling, S. D. Katz, S. Krieg, C. Ratti, and K. K. Szabó, Is there still any T_c mystery in lattice QCD? Results with physical masses in the continuum limit III, J. High Energy Phys. 09 (2010) 073.

[4] Y. Aoki, Z. Fodor, S. D. Katz, and K. K. Szabó, The QCD transition temperature: Results with physical masses in the continuum limit, Phys. Lett. B **643**, 46 (2006).

[5] Y. Aoki, S. Borsányi, S. Dürr, Z. Fodor, S. D. Katz, S. Krieg, and K. K. Szabó, The QCD transition temperature: results with physical masses in the continuum limit II, J. High Energy Phys. 06 (2009) 088.

[6] J. Cleymans, I. Kraus, H. Oeschler, K. Redlich, and S. Wheaton, Statistical model predictions for particle ratios at $\sqrt{s_{NN}}$ = 5.5 TeV, Phys. Rev. C **74**, 034903 (2006).

[7] J. Rafelski, J. Letessier, and G. Torrieri, Centrality dependence of bulk fireball properties in $\sqrt{s_{NN}}$ = 200 GeV Au-Au collisions, Phys. Rev. C **72**, 024905 (2005).

[8] M. Petráň and J. Rafelski, Universal hadronization condition in heavy ion collisions at $\sqrt{s_{NN}}$ = 62 GeV and at $\sqrt{s_{NN}}$ = 2.76 TeV, Phys. Rev. C **88**, 021901(R) (2013).

[9] M. Petráň, J. Letessier, V. Petráček, and J. Rafelski, Hadron production and quark-gluon plasma hadronization in Pb-Pb collisions at $\sqrt{s_{NN}}$ = 2.76 TeV, Phys. Rev. C **88**, 034907 (2013).

[10] A. Andronic, P. Braun-Munzinger, and J. Stachel, Thermal hadron production in relativistic nuclear collisions: The hadron mass spectrum, the horn, and the QCD phase transition, Phys. Lett. B **673**, 142 (2009); Erratum to: Thermal hadron production in relativistic nuclear collisions: The hadron mass spectrum, the horn, and the QCD phase transition [Phys. Lett. B **673**, 142 (2009)] **678**, 516 (2009).

[11] A. Andronic, P. Braun-Munzinger, and J. Stachel, The thermal model on the verge of the ultimate test: Particle production in Pb-Pb collisions at the LHC, J. Phys. G **38**, 124081 (2011).

[12] F. Becattini, M. Gaździcki, A. Keränen, J. Manninen, and R. Stock, Chemical equilibrium study in nucleus-nucleus collisions at relativistic energies, Phys. Rev. C **69**, 024905 (2004).

[13] F. Becattini, P. Castorina, A. Milov, and H. Satz, A comparative analysis of statistical hadron production, Eur. Phys. J. C **66**, 377 (2010).

[14] M. Bleicher and H. Stöcker, Dynamics and freeze-out of hadron resonances at RHIC, J. Phys. G **30**, S111 (2004).

[15] C. Markert, G. Torrieri, and J. Rafelski, Strange hadron resonances: Freezeout probes in heavy ion collisions, AIP Conf. Proc. **631**, 533 (2002).

[16] S. Vogel and M. Bleicher, Resonance absorption and regeneration in relativistic heavy ion collisions, in *Proceedings of the XLIII International Winter Meeting on Nuclear Physics, Bormio, Italy, March 14–19, 2005, Ricerca Scientifica ed Educazione Permanente, Supplemento N. 124*, edited by I. Iori and A. Bortolotti (Università degli Studi di Milano, Milan, 2005), pp. 116–119.

[17] M. Bleicher and J. Aichelin, Strange resonance production: Probing chemical and thermal freeze-out in relativistic heavy ion collisions, Phys. Lett. B **530**, 81 (2002).

[18] M. J. Matison, A. Barbaro-Galtieri, M. Alston-Garnjost, S. M. Flatté, J. H. Friedman, G. R. Lynch, M. S. Rabin, and F. T. Solmitz, Study of $K^+\pi^-$ scattering in the reaction $K^+p \to K^+\pi^-\Delta^{++}$ at 12 GeV/c, Phys. Rev. D **9**, 1872 (1974).

[19] S. D. Protopopescu, M. Alston-Garnjost, A. Barbaro-Galtieri, S. M. Flatté, J. H. Friedman, T. A. Lasinski, G. R. Lynch, M. S. Rabin, and F. T. Solmitz, $\pi\pi$ Partial-wave analysis from reactions $\pi^+p \to \pi^+\pi^-\Delta^{++}$ and $\pi^+p \to K^+K^-\Delta^{++}$ at 7.1 GeV/c, Phys. Rev. D **7**, 1279 (1973).

[20] S. A. Bass *et al.*, Microscopic models for ultrarelativistic heavy ion collisions, Prog. Part. Nucl. Phys. **41**, 255 (1998).

[21] M. Bleicher *et al.*, Relativistic hadron-hadron collisions in the ultra-relativistic quantum molecular dynamics model, J. Phys. G **25**, 1859 (1999).

[22] G. Torrieri and J. Rafelski, Strange hadron resonances as a signature of freeze-out dynamics, Phys. Lett. B **509**, 239 (2001).

[23] J. Rafelski, J. Letessier, and G. Torrieri, Strange hadrons and their resonances: A diagnostic tool of quark-gluon plasma freeze-out dynamics, Phys. Rev. C **64**, 054907 (2001); Erratum to: Strange hadrons and their resonances: A diagnostic tool of quark-gluon plasma freeze-out dynamics [Phys. Rev. C **64**, 054907 (2001)] **65**, 069902(E) (2002).

[24] P. Petreczky, Lattice QCD at finite temperature, Nucl. Phys. A **785**, 10 (2007).

[25] G. E. Brown and M. Rho, On the manifestation of chiral symmetry in nuclei and dense nuclear matter, Phys. Rep. **363**, 85 (2002).

[26] R. Rapp, J. Wambach, and H. van Hees, The chiral restoration transition of QCD and low mass dileptons, in *Relativistic Heavy Ion Physics*, edited by R. Stock (Springer, Berlin, 2010), pp. 134–175.

[27] S. J. Brodsky and G. F. de Teramond, Spin correlations, QCD color transparency, and heavy-quark thresholds in proton-proton scattering, Phys. Rev. Lett. **60**, 1924 (1988).

[28] V. L. Eletsky, M. Belkacem, P. J. Ellis, and J. I. Kapusta, Properties of ρ and ω mesons at finite temperature and density as inferred from experiment, Phys. Rev. C **64**, 035202 (2001).

[29] K. Aamodt *et al.* (ALICE Collaboration), The ALICE experiment at the CERN LHC, J. Instrum. **3**, S08002 (2008).

[30] E. Abbas *et al.* (ALICE Collaboration), Performance of the ALICE VZERO system, J. Instrum. **8**, P10016 (2013).

[31] K. Aamodt *et al.* (ALICE Collaboration), Centrality dependence of the charged-particle multiplicity density at midrapidity in Pb-Pb collisions at $\sqrt{s_{NN}} = 2.76$ TeV, Phys. Rev. Lett. **106**, 032301 (2011).

[32] B. Abelev *et al.* (ALICE Collaboration), Centrality determination of Pb-Pb collisions at $\sqrt{s_{NN}} = 2.76$ TeV with ALICE, Phys. Rev. C **88**, 044909 (2013).

[33] J. Alme *et al.*, The ALICE TPC, a large 3-dimensional tracking device with fast readout for ultra-high multiplicity events, Nucl. Instrum. Methods Phys. Res. A **622**, 316 (2010).

[34] B. Abelev *et al.* (ALICE Collaboration), Centrality dependence of π, K, and p production in Pb-Pb collisions at $\sqrt{s_{NN}} = 2.76$ TeV, Phys. Rev. C **88**, 044910 (2013).

[35] J. Beringer *et al.* (Particle Data Group), Review of particle physics, Phys. Rev. D **86**, 010001 (2012).

[36] J. Adams *et al.* (STAR Collaboration), $K(892)^*$ resonance production in Au+Au and $p + p$ collisions at $\sqrt{s_{NN}} = 200$ GeV, Phys. Rev. C **71**, 064902 (2005).

[37] Z. Xu, Resonances at RHIC, J. Phys. G **30**, S325 (2004).

[38] P. F. Kolb and M. Prakash, Spectroscopy of resonance decays in high-energy heavy-ion experiments, Phys. Rev. C **67**, 044902 (2003).

[39] E. V. Shuryak and G. E. Brown, Matter-induced modification of resonances at RHIC freezeout, Nucl. Phys. A **717**, 322 (2003).

[40] X.-N. Wang and M. Gyulassy, HIJING: A Monte Carlo model for multiple jet production in pp, pA, and AA collisions, Phys. Rev. D **44**, 3501 (1991).

[41] R. Brun, F. Carminati, and S. Giani, GEANT–Detector Description and Simulation Tool, CERN Program Library Long Writeup W5013 (CERN, Geneva, 1994).

[42] B. Abelev *et al.* (ALICE Collaboration), Centrality dependence of charged particle production at large transverse momentum in Pb-Pb collisions at $\sqrt{s_{NN}} = 2.76$ TeV, Phys. Lett. B **720**, 52 (2013).

[43] K. Aamodt *et al.* (ALICE Collaboration), Strange particle production in proton-proton collisions at $\sqrt{s} = 900$ GeV with ALICE at the LHC, Eur. Phys. J. C **71**, 1594 (2011).

[44] E. Schnedermann, J. Sollfrank, and U. Heinz, Thermal phenomenology of hadrons from $200A$ GeV S+S collisions, Phys. Rev. C **48**, 2462 (1993).

[45] J. Adams *et al.* (STAR Collaboration), Experimental and theoretical challenges in the search for the quark-gluon plasma: The STAR Collaboration's critical assessment of the evidence from RHIC collisions, Nucl. Phys. A **757**, 102 (2005).

[46] S. S. Adler *et al.* (PHENIX Collaboration), Production of ϕ mesons at midrapidity in $\sqrt{s_{NN}} = 200$ GeV Au+Au collisions at relativistic energies, Phys. Rev. C **72**, 014903 (2005).

[47] U. Heinz, Concepts of heavy-ion physics, in *Proceedings of the 2nd CERN-CLAF School of High-energy Physics, Mexico City, Mexico, June 1–14 2003*, edited by N. Ellis (CERN, Geneva, 2006), pp. 165–237.

[48] C. Tsallis, Possible generalization of Boltzmann-Gibbs statistics, J. Stat. Phys. **52**, 479 (1988).

[49] B. I. Abelev *et al.* (STAR Collaboration), Strange particle production in $p + p$ collisions at $\sqrt{s} = 200$ GeV, Phys. Rev. C **75**, 064901 (2007).

[50] M. M. Aggarwal *et al.* (STAR Collaboration), K^{*0} production in Cu+Cu and Au+Au collisions at $\sqrt{s_{NN}} = 62.4$ GeV and 200 GeV, Phys. Rev. C **84**, 034909 (2011).

[51] B. I. Abelev *et al.* (STAR Collaboration), Measurements of ϕ meson production in relativistic heavy-ion collisions at the BNL Relativistic Heavy Ion Collider (RHIC), Phys. Rev. C **79**, 064903 (2009).

[52] C. Alt *et al.* (NA49 Collaboration), Energy dependence of ϕ meson production in central Pb+Pb collisions at $\sqrt{s_{NN}} = 6$ to 17 GeV, Phys. Rev. C **78**, 044907 (2008).

[53] K. Aamodt *et al.* (ALICE Collaboration), Charged-particle multiplicity measurement in proton-proton collisions at $\sqrt{s} = 7$ TeV with ALICE at LHC, Eur. Phys. J. C **68**, 345 (2010).

[54] B. Abelev *et al.* (ALICE Collaboration), Production of $K^*(892)^0$ and $\phi(1020)$ in pp collisions at $\sqrt{s} = 7$ TeV, Eur. Phys. J. C **72**, 2183 (2012).

[55] B. Abelev *et al.* (ALICE Collaboration), Measurement of pion, kaon and proton production in proton-proton collisions at $\sqrt{s} = 7$ TeV (unpublished).

[56] J. Stachel, A. Andronic, P. Braun-Munzinger, and K. Redlich, Confronting LHC data with the statistical hadronization model, J. Phys.: Conf. Ser. **509**, 012019 (2014).

[57] S. A. Bass, A. Dumitru, M. Bleicher, L. Bravina, E. Zabrodin, H. Stöcker, and W. Greiner, Hadronic freeze-out following a first order hadronization phase transition in ultrarelativistic heavy-ion collisions, Phys. Rev. C **60**, 021902(R) (1999).

[58] K. Aamodt *et al.* (ALICE Collaboration), Two-pion Bose-Einstein correlations in central Pb-Pb collisions at $\sqrt{s_{NN}} = 2.76$ TeV, Phys. Lett. B **696**, 328 (2011).

[59] M. A. Lisa, S. Pratt, R. Soltz, and U. Wiedemann, Femtoscopy in relativistic heavy ion collisions: Two decades of progress, Annu. Rev. Nucl. Part. Sci. **55**, 357 (2005).

[60] B. I. Abelev *et al.* (STAR Collaboration), Hadronic resonance production in $d + $Au collisions at $\sqrt{s_{NN}} = 200$ GeV measured at the BNL Relativistic Heavy Ion Collider, Phys. Rev. C **78**, 044906 (2008).

[61] J. Adams *et al.* (STAR Collaboration), ϕ meson production in Au+Au and $p + p$ collisions at $\sqrt{s_{NN}} = 200$ GeV, Phys. Lett. B **612**, 181 (2005).

[62] S. V. Afanasiev *et al.* (NA49 Collaboration), Production of ϕ-mesons in $p + p$, $p + $Pb and central Pb+Pb collisions at $E_{beam} = 158$ A GeV, Phys. Lett. B **491**, 59 (2000).

[63] S. V. Afanasiev *et al.* (NA49 Collaboration), Energy dependence of pion and kaon production in central Pb+Pb collisions, Phys. Rev. C **66**, 054902 (2002).

[64] C. Adler *et al.* (STAR Collaboration), Midrapidity ϕ production in Au+Au collisions at $\sqrt{s_{NN}} = 130$ GeV, Phys. Rev. C **65**, 041901(R) (2002).

[65] A. Adare *et al.* (PHENIX Collaboration), Measurement of neutral mesons in $p + p$ collisions at $\sqrt{s} = 200$ GeV and scaling properties of hadron production, Phys. Rev. D **83**, 052004 (2011).

[66] A. Adare *et al.* (PHENIX Collaboration), Identified charged hadron production in $p + p$ collisions at $\sqrt{s} = 200$ and 62.4 GeV, Phys. Rev. C **83**, 064903 (2011).

[67] K. Aamodt *et al.* (ALICE Collaboration), Production of pions, kaons and protons in pp collisions at $\sqrt{s} = 900$ GeV with ALICE at the LHC, Eur. Phys. J. C **71**, 1655 (2011).

[68] B. I. Abelev *et al.* (STAR Collaboration), Systematic measurements of identified particle spectra in pp, $d + $Au, and Au+Au collisions at the STAR detector, Phys. Rev. C **79**, 034909 (2009).

[69] M. M. Aggarwal *et al.* (STAR Collaboration), Scaling properties at freeze-out in relativistic heavy-ion collisions, Phys. Rev. C **83**, 034910 (2011).

[70] B. I. Abelev *et al.* (STAR Collaboration), Strange baryon resonance production in $\sqrt{s_{NN}} = 200$ GeV $p + p$ and Au+Au collisions, Phys. Rev. Lett. **97**, 132301 (2006).

[71] B. Abelev *et al.* (ALICE Collaboration), Multi-strange baryon production at mid-rapidity in Pb-Pb collisions at $\sqrt{s_{NN}} = 2.76$ TeV, Phys. Lett. B **728**, 216 (2013); Corrigendum to: Multi-strange baryon production at mid-rapidity in Pb-Pb collisions at $\sqrt{s_{NN}} = 2.76$ TeV [Phys. Lett. B **728**, 216 (2014)] **734**, 409 (2014).

[72] P. Bożek and I. Wyskiel-Piekarska, Particle spectra in Pb-Pb collisions at $\sqrt{s_{NN}} = 2.76$ TeV, Phys. Rev. C **85**, 064915 (2012).

[73] Z. Qui, C. Shen, and U. Heinz, Hydrodynamic elliptic and triangular flow in Pb-Pb collisions at $\sqrt{s_{NN}} = 2.76A$ TeV, Phys. Lett. B **707**, 151 (2012).

[74] C. Shen, U. Heinz, P. Huovinen, and H. Song, Radial and elliptic flow in Pb+Pb collisions at energies available at the CERN Large Hadron Collider from viscous hydrodynamics, Phys. Rev. C **84**, 044903 (2011).

[75] H. Song, S. A. Bass, and U. Heinz, Spectra and elliptic flow for identified hadrons in 2.76A TeV Pb+Pb collisions, Phys. Rev. C **89**, 034919 (2014).

[76] H. Song, Hydrodynamic modeling and the QGP shear viscosity, Eur. Phys. J. A **48**, 163 (2012).

[77] Y. A. Karpenko and Y. M. Sinyukov, Femtoscopic scales in central $A + A$ collisions at RHIC and LHC energies in a hydrokinetic model, J. Phys. G **38**, 124059 (2011).

[78] I. A. Karpenko, Y. M. Sinyukov, and K. Werner, Uniform description of bulk observables in the hydrokinetic model of $A + A$ collisions at the BNL Relativistic Heavy Ion Collider and the CERN Large Hadron Collider, Phys. Rev. C **87**, 024914 (2013).

[79] B. Abelev *et al.* (ALICE Collaboration), Multi-strange baryon production in pp collisions at $\sqrt{s} = 7$ TeV with ALICE, Phys. Lett. B **712**, 309 (2012).

[80] V. Topor Pop, M. Gyulassy, J. Barrette, C. Gale, and A. Warburton, Strong longitudinal color-field effects in pp collisions at energies available at the CERN Large Hadron Collider, Phys. Rev. C **83**, 024902 (2011).

[81] V. Topor Pop, M. Gyulassy, J. Barrette, and C. Gale, Baryon anomaly and strong color fields in Pb+Pb collisions at 2.76A TeV at the CERN Large Hadron Collider, Phys. Rev. C **84**, 044909 (2011).

[82] N. Armesto *et al.*, Heavy-ion collisions at the LHC–Last call for predictions, J. Phys. G **35**, 054001 (2008).

[83] V. Topor Pop, M. Gyulassy, J. Barrette, C. Gale, and A. Warburton, Hyperon/meson ratios in rare high-multiplicity pp collisions at energies available at the Large Hadron Collider, and potential signatures for mini-quark-gluon plasma formation, Phys. Rev. C **86**, 044902 (2012).

[84] V. Topor Pop, M. Gyulassy, J. Barrette, C. Gale, and M. Petrovici, Open charm production in $p + p$ and Pb+Pb collisions at the CERN Large Hadron Collider, J. Phys. G **41**, 115101 (2014).

[85] Y. G. Ma, ϕ-meson production and partonic collectivity at RHIC, J. Phys. G **32**, S373 (2006).

[86] B. Abelev *et al.* (ALICE Collaboration), Production of charged pions, kaons and protons at large transverse momenta in pp and Pb-Pb collisions at $\sqrt{s_{NN}} = 2.76$ TeV, Phys. Lett. B **736**, 196 (2014).

[87] B. I. Abelev *et al.* (STAR Collaboration), Identified baryon and meson distributions at large transverse momenta from Au+Au collisions at $\sqrt{s_{NN}} = 200$ GeV, Phys. Rev. Lett. **97**, 152301 (2006).

[88] J. Adams *et al.* (STAR Collaboration), Particle-type dependence of azimuthal anisotropy and nuclear modification of particle production in Au+Au collisions at $\sqrt{s_{NN}} = 200$ GeV, Phys. Rev. Lett. **92**, 052302 (2004).

[89] B. I. Abelev *et al.* (STAR Collaboration), Partonic flow and ϕ-meson production in Au+Au collisions at $\sqrt{s_{NN}} = 200$ GeV, Phys. Rev. Lett. **99**, 112301 (2007).

[90] J. Adams *et al.* (STAR Collaboration), Scaling properties of hyperon production in Au+Au collisions at $\sqrt{s_{NN}} = 200$ GeV, Phys. Rev. Lett. **98**, 062301 (2007).

[91] R. Fries, V. Greco, and P. Sorensen, Coalescence models for hadron formation from quark-gluon plasma, Annu. Rev. Nucl. Part. Sci **58**, 177 (2008).

[92] F. Antinori *et al.* (NA57 Collaboration), Strangeness enhancements at central rapidity in 40 A GeV/c Pb-Pb collisions, J. Phys. G **37**, 045105 (2010).

[93] F. Antinori *et al.* (NA57 Collaboration), Enhancement of hyperon production at central rapidity in 158 A GeV/c Pb-Pb collisions, J. Phys. G **32**, 427 (2006).

[94] E. Andersen *et al.* (WA97 Collaboration), Strangeness enhancement at mid-rapidity in Pb-Pb collisions at 158 A GeV/c, Phys. Lett. B **449**, 401 (1999).

[95] C. Alt *et al.* (NA49 Collaboration), Ω^- and $\overline{\Omega}^+$ production in central Pb+Pb collisions at 40 and 158*A* GeV, Phys. Rev. Lett. **94**, 192301 (2005).

[96] C. Alt *et al.* (NA49 Collaboration), Energy dependence of Λ and Ξ production in central Pb+Pb collisions at 20*A*, 30*A*, 40*A*, 80*A*, and 158*A* GeV measured at the CERN Super Proton Synchrotron, Phys. Rev. C **78**, 034918 (2008).

[97] T. Anticic *et al.* (NA49 Collaboration), System-size dependence of Λ and Ξ production in nucleus-nucleus collisions at 40*A* and 158*A* GeV measured at the CERN Super Proton Synchrotron, Phys. Rev. C **80**, 034906 (2009).

[98] J. Adams *et al.* (STAR Collaboration), Multistrange baryon production in Au-Au collisions at $\sqrt{s_{NN}} = 130$ GeV, Phys. Rev. Lett. **92**, 182301 (2004).

[99] B. I. Abelev *et al.* (STAR Collaboration), Enhanced strange baryon production in Au+Au collisions compared to $p + p$ at $\sqrt{s_{NN}} = 200$ GeV, Phys. Rev. C **77**, 044908 (2008).

[100] K. Aamodt *et al.* (ALICE Collaboration), Charged-particle multiplicity density at midrapidity in central Pb-Pb collisions at $\sqrt{s_{NN}} = 2.76$ TeV, Phys. Rev. Lett. **105**, 252301 (2010).

[101] B. Abelev *et al.* (ALICE Collaboration), K_S^0 and Λ production in Pb-Pb collisions at $\sqrt{s_{NN}} = 2.76$ TeV, Phys. Rev. Lett. **111**, 222301 (2013).

[102] V. Khachatryan *et al.* (CMS Collaboration), Strange particle production in pp collisions at $\sqrt{s} = 0.9$ and 7 TeV, J. High Energy Phys. 05 (2011) 064.

[103] B. I. Abelev *et al.* (STAR Collaboration), Energy and system size dependence of ϕ meson production in Cu+Cu and Au+Au collisions, Phys. Lett. B **673**, 183 (2009).

[104] G. Agakishiev *et al.* (STAR Collaboration), Strangeness enhancement in Cu-Cu and Au-Au collisions at $\sqrt{s_{NN}} = 200$ GeV, Phys. Rev. Lett. **108**, 072301 (2012).

[105] I. Kraus, J. Cleymans, H. Oeschler, K. Redlich, and S. Wheaton, Chemical equilibrium in collisions of small systems, Phys. Rev. C **76**, 064903 (2007).

B. Abelev,[1,†] J. Adam,[2] D. Adamová,[3] M. M. Aggarwal,[4] M. Agnello,[5,6] A. Agostinelli,[7] N. Agrawal,[8] Z. Ahammed,[9] N. Ahmad,[10] A. Ahmad Masoodi,[10] I. Ahmed,[11] S. U. Ahn,[12] S. A. Ahn,[12] I. Aimo,[5,6] S. Aiola,[13] M. Ajaz,[11] A. Akindinov,[14] D. Aleksandrov,[15] B. Alessandro,[5] D. Alexandre,[16] A. Alici,[17,18] A. Alkin,[19] J. Alme,[20] T. Alt,[21] V. Altini,[22] S. Altinpinar,[23] I. Altsybeev,[24] C. Alves Garcia Prado,[25] C. Andrei,[26] A. Andronic,[27] V. Anguelov,[28] J. Anielski,[29] T. Antičić,[30] F. Antinori,[31] P. Antonioli,[18] L. Aphecetche,[32] H. Appelshäuser,[33] N. Arbor,[34] S. Arcelli,[7] N. Armesto,[35] R. Arnaldi,[5] T. Aronsson,[13] I. C. Arsene,[27] M. Arslandok,[33] A. Augustinus,[36] R. Averbeck,[27] T. C. Awes,[37] M. D. Azmi,[38] M. Bach,[21] A. Badalà,[39] Y. W. Baek,[40,41] S. Bagnasco,[5] R. Bailhache,[33] R. Bala,[42] A. Baldisseri,[43] F. Baltasar Dos Santos Pedrosa,[36] R. C. Baral,[44] R. Barbera,[45] F. Barile,[22] G. G. Barnaföldi,[46] L. S. Barnby,[16] V. Barret,[40] J. Bartke,[47] M. Basile,[7] N. Bastid,[40] S. Basu,[9] B. Bathen,[29] G. Batigne,[32] B. Batyunya,[48] P. C. Batzing,[49] C. Baumann,[33] I. G. Bearden,[50] H. Beck,[33] C. Bedda,[6] N. K. Behera,[8] I. Belikov,[51] F. Bellini,[7] R. Bellwied,[52] E. Belmont-Moreno,[53] G. Bencedi,[46] S. Beole,[54] I. Berceanu,[26] A. Bercuci,[26] Y. Berdnikov,[55,56] D. Berenyi,[46] R. A. Bertens,[57] D. Berzano,[54] L. Betev,[36] A. Bhasin,[42] I. R. Bhat,[42] A. K. Bhati,[4] B. Bhattacharjee,[58] J. Bhom,[59] L. Bianchi,[54] N. Bianchi,[60] C. Bianchin,[57] J. Bielčík,[2] J. Bielčíková,[3] A. Bilandzic,[50] S. Bjelogrlic,[57] F. Blanco,[61] D. Blau,[15] C. Blume,[33] F. Bock,[28,62] A. Bogdanov,[63] H. Bøggild,[50] M. Bogolyubsky,[64] L. Boldizsár,[46] M. Bombara,[65] J. Book,[33] H. Borel,[43] A. Borissov,[66] F. Bossú,[67] M. Botje,[68] E. Botta,[54] S. Böttger,[69] P. Braun-Munzinger,[27] M. Bregant,[25] T. Breitner,[69] T. A. Broker,[33] T. A. Browning,[70] M. Broz,[71,2] E. Bruna,[5] G. E. Bruno,[22] D. Budnikov,[72] H. Buesching,[33] S. Bufalino,[5] P. Buncic,[36] O. Busch,[28] Z. Buthelezi,[67] D. Caffarri,[73] X. Cai,[74] H. Caines,[13] A. Caliva,[57] E. Calvo Villar,[75] P. Camerini,[76] F. Carena,[36] W. Carena,[36] J. Castillo Castellanos,[43] E. A. R. Casula,[77] V. Catanescu,[26] C. Cavicchioli,[36] C. Ceballos Sanchez,[78] J. Cepila,[2] P. Cerello,[5] B. Chang,[79] S. Chapeland,[36] J. L. Charvet,[43] S. Chattopadhyay,[9] S. Chattopadhyay,[80] V. Chelnokov,[19] M. Cherney,[81] C. Cheshkov,[82] B. Cheynis,[82] V. Chibante Barroso,[36] D. D. Chinellato,[52] P. Chochula,[36] M. Chojnacki,[50] S. Choudhury,[9] P. Christakoglou,[68] C. H. Christensen,[50] P. Christiansen,[83] T. Chujo,[59] S. U. Chung,[84] C. Cicalo,[85] L. Cifarelli,[17,7] F. Cindolo,[18] J. Cleymans,[38] F. Colamaria,[22] D. Colella,[22] A. Collu,[77] M. Colocci,[7] G. Conesa Balbastre,[34] Z. Conesa del Valle,[86] M. E. Connors,[13] J. G. Contreras,[87] T. M. Cormier,[66] Y. Corrales Morales,[54] P. Cortese,[88] I. Cortés Maldonado,[89] M. R. Cosentino,[25] F. Costa,[36] P. Crochet,[40] R. Cruz Albino,[87] E. Cuautle,[90] L. Cunqueiro,[60] A. Dainese,[31] R. Dang,[74] A. Danu,[91] D. Das,[80] I. Das,[86] K. Das,[80] S. Das,[92] A. Dash,[93] S. Dash,[8] S. De,[9] H. Delagrange,[32,‡] A. Deloff,[94] E. Dénes,[46] G. D'Erasmo,[22] A. De Caro,[95,17] G. de Cataldo,[96] J. de Cuveland,[21] A. De Falco,[77] D. De Gruttola,[95,17] N. De Marco,[5] S. De Pasquale,[95] R. de Rooij,[57] M. A. Diaz Corchero,[61] T. Dietel,[29] R. Divià,[36] D. Di Bari,[22] S. Di Liberto,[97] A. Di Mauro,[36] P. Di Nezza,[60] Ø. Djuvsland,[23] A. Dobrin,[57] T. Dobrowolski,[94] D. Domenicis Gimenez,[25] B. Dönigus,[33] O. Dordic,[49] A. K. Dubey,[9] A. Dubla,[57] L. Ducroux,[82] P. Dupieux,[40] A. K. Dutta Majumdar,[80] R. J. Ehlers,[13] D. Elia,[96] H. Engel,[69] B. Erazmus,[36,32] H. A. Erdal,[20] D. Eschweiler,[21] B. Espagnon,[86] M. Esposito,[36] M. Estienne,[32] S. Esumi,[59] D. Evans,[16] S. Evdokimov,[64] D. Fabris,[31] J. Faivre,[34] D. Falchieri,[7] A. Fantoni,[60] M. Fasel,[28] D. Fehlker,[23] L. Feldkamp,[29] D. Felea,[91] A. Feliciello,[5] G. Feofilov,[24] J. Ferencei,[3] A. Fernández Téllez,[89] E. G. Ferreiro,[35] A. Ferretti,[54] A. Festanti,[73] J. Figiel,[47] M. A. S. Figueredo,[98] S. Filchagin,[72] D. Finogeev,[99] F. M. Fionda,[22] E. M. Fiore,[22] E. Floratos,[100] M. Floris,[36] S. Foertsch,[67] P. Foka,[27] S. Fokin,[15] E. Fragiacomo,[101] A. Francescon,[36,73] U. Frankenfeld,[27] U. Fuchs,[36] C. Furget,[34] M. Fusco Girard,[95] J. J. Gaardhøje,[50] M. Gagliardi,[54] A. M. Gago,[75] M. Gallio,[54] D. R. Gangadharan,[102] P. Ganoti,[37] C. Garabatos,[27] E. Garcia-Solis,[103] C. Gargiulo,[36] I. Garishvili,[1] J. Gerhard,[21] M. Germain,[32] A. Gheata,[36] M. Gheata,[36,91] B. Ghidini,[22] P. Ghosh,[9] S. K. Ghosh,[92] P. Gianotti,[60] P. Giubellino,[36] E. Gladysz-Dziadus,[47] P. Glässel,[28] A. Gomez Ramirez,[69] P. González-Zamora,[61] S. Gorbunov,[21] L. Görlich,[47] S. Gotovac,[104]

L. K. Graczykowski,[105] A. Grelli,[57] A. Grigoras,[36] C. Grigoras,[36] V. Grigoriev,[63] A. Grigoryan,[106] S. Grigoryan,[48] B. Grinyov,[19] N. Grion,[101] J. F. Grosse-Oetringhaus,[36] J.-Y. Grossiord,[82] R. Grosso,[36] F. Guber,[99] R. Guernane,[34] B. Guerzoni,[7] M. Guilbaud,[82] K. Gulbrandsen,[50] H. Gulkanyan,[106] T. Gunji,[107] A. Gupta,[42] R. Gupta,[42] K. H. Khan,[11] R. Haake,[29] Ø. Haaland,[23] C. Hadjidakis,[86] M. Haiduc,[91] H. Hamagaki,[107] G. Hamar,[46] L. D. Hanratty,[16] A. Hansen,[50] J. W. Harris,[13] H. Hartmann,[21] A. Harton,[103] D. Hatzifotiadou,[18] S. Hayashi,[107] S. T. Heckel,[33] M. Heide,[29] H. Helstrup,[20] A. Herghelegiu,[26] G. Herrera Corral,[87] B. A. Hess,[108] K. F. Hetland,[20] B. Hicks,[13] B. Hippolyte,[51] J. Hladky,[109] P. Hristov,[36] M. Huang,[23] T. J. Humanic,[102] D. Hutter,[21] D. S. Hwang,[110] R. Ilkaev,[72] I. Ilkiv,[94] M. Inaba,[59] G. M. Innocenti,[54] C. Ionita,[36] M. Ippolitov,[15] M. Irfan,[10] M. Ivanov,[27] V. Ivanov,[56] O. Ivanytskyi,[19] A. Jachołkowski,[45] P. M. Jacobs,[62] C. Jahnke,[25] H. J. Jang,[12] M. A. Janik,[105] P. H. S. Y. Jayarathna,[52] S. Jena,[52] R. T. Jimenez Bustamante,[90] P. G. Jones,[16] H. Jung,[41] A. Jusko,[16] V. Kadyshevskiy,[48] S. Kalcher,[21] P. Kalinak,[111] A. Kalweit,[36] J. Kamin,[33] J. H. Kang,[112] V. Kaplin,[63] S. Kar,[9] A. Karasu Uysal,[113] O. Karavichev,[99] T. Karavicheva,[99] E. Karpechev,[99] U. Kebschull,[69] R. Keidel,[114] M. M. Khan,[115,10] P. Khan,[80] S. A. Khan,[9] A. Khanzadeev,[56] Y. Kharlov,[64] B. Kileng,[20] B. Kim,[112] D. W. Kim,[12,41] D. J. Kim,[79] J. S. Kim,[41] M. Kim,[41] M. Kim,[112] S. Kim,[110] T. Kim,[112] S. Kirsch,[21] I. Kisel,[21] S. Kiselev,[14] A. Kisiel,[105] G. Kiss,[46] J. L. Klay,[116] J. Klein,[28] C. Klein-Bösing,[29] A. Kluge,[36] M. L. Knichel,[27] A. G. Knospe,[117] C. Kobdaj,[36,118] M. K. Köhler,[27] T. Kollegger,[21] A. Kolojvari,[24] V. Kondratiev,[24] N. Kondratyeva,[63] A. Konevskikh,[99] V. Kovalenko,[24] M. Kowalski,[47] S. Kox,[34] G. Koyithatta Meethaleveedu,[8] J. Kral,[79] I. Králik,[111] F. Kramer,[33] A. Kravčáková,[65] M. Krelina,[2] M. Kretz,[21] M. Krivda,[16,111] F. Krizek,[3] M. Krus,[2] E. Kryshen,[36,56] M. Krzewicki,[27] V. Kučera,[3] Y. Kucheriaev,[15,‡] T. Kugathasan,[36] C. Kuhn,[51] P. G. Kuijer,[68] I. Kulakov,[33] J. Kumar,[8] P. Kurashvili,[94] A. Kurepin,[99] A. B. Kurepin,[99] A. Kuryakin,[72] S. Kushpil,[3] M. J. Kweon,[28] Y. Kwon,[112] P. Ladron de Guevara,[90] C. Lagana Fernandes,[25] I. Lakomov,[86] R. Langoy,[119] C. Lara,[69] A. Lardeux,[32] A. Lattuca,[54] S. L. La Pointe,[57] P. La Rocca,[45] R. Lea,[76] G. R. Lee,[16] I. Legrand,[36] J. Lehnert,[33] R. C. Lemmon,[120] V. Lenti,[96] E. Leogrande,[57] M. Leoncino,[54] I. León Monzón,[121] P. Lévai,[46] S. Li,[74,40] J. Lien,[119] R. Lietava,[16] S. Lindal,[49] V. Lindenstruth,[21] C. Lippmann,[27] M. A. Lisa,[102] H. M. Ljunggren,[83] D. F. Lodato,[57] P. I. Loenne,[23] V. R. Loggins,[66] V. Loginov,[63] D. Lohner,[28] C. Loizides,[62] X. Lopez,[40] E. López Torres,[78] X.-G. Lu,[28] P. Luettig,[33] M. Lunardon,[73] J. Luo,[74] G. Luparello,[57] C. Luzzi,[36] R. Ma,[13] A. Maevskaya,[99] M. Mager,[36] D. P. Mahapatra,[44] A. Maire,[28] R. D. Majka,[13] M. Malaev,[56] I. Maldonado Cervantes,[90] L. Malinina,[122,48] D. Mal'Kevich,[14] P. Malzacher,[27] A. Mamonov,[72] L. Manceau,[5] V. Manko,[15] F. Manso,[40] V. Manzari,[96] M. Marchisone,[40,54] J. Mareš,[109] G. V. Margagliotti,[76] A. Margotti,[18] A. Marín,[27] C. Markert,[117] M. Marquard,[33] I. Martashvili,[123] N. A. Martin,[27] P. Martinengo,[36] M. I. Martínez,[89] G. Martínez García,[32] J. Martin Blanco,[32] Y. Martynov,[19] A. Mas,[32] S. Masciocchi,[27] M. Masera,[54] A. Masoni,[85] L. Massacrier,[32] A. Mastroserio,[22] A. Matyja,[47] C. Mayer,[47] J. Mazer,[123] M. A. Mazzoni,[97] F. Meddi,[124] A. Menchaca-Rocha,[53] J. Mercado Pérez,[28] M. Meres,[71] Y. Miake,[59] K. Mikhaylov,[48,14] L. Milano,[36] J. Milosevic,[125,49] A. Mischke,[57] A. N. Mishra,[126] D. Miśkowiec,[27] C. M. Mitu,[91] J. Mlynarz,[66] B. Mohanty,[127,9] L. Molnar,[51] L. Montaño Zetina,[87] E. Montes,[61] M. Morando,[73] D. A. Moreira De Godoy,[25] S. Moretto,[73] A. Morreale,[79] A. Morsch,[36] V. Muccifora,[60] E. Mudnic,[104] S. Muhuri,[9] M. Mukherjee,[9] H. Müller,[36] M. G. Munhoz,[25] S. Murray,[38] L. Musa,[36] J. Musinsky,[111] B. K. Nandi,[8] R. Nania,[18] E. Nappi,[96] C. Nattrass,[123] T. K. Nayak,[9] S. Nazarenko,[72] A. Nedosekin,[14] M. Nicassio,[27] M. Niculescu,[36,91] B. S. Nielsen,[50] S. Nikolaev,[15] S. Nikulin,[15] V. Nikulin,[56] B. S. Nilsen,[81] F. Noferini,[17,18] P. Nomokonov,[48] G. Nooren,[57] A. Nyanin,[15] J. Nystrand,[23] H. Oeschler,[28] S. Oh,[13] S. K. Oh,[128,41] A. Okatan,[113] L. Olah,[46] J. Oleniacz,[105] A. C. Oliveira Da Silva,[25] J. Onderwaater,[27] C. Oppedisano,[5] A. Ortiz Velasquez,[83] A. Oskarsson,[83] J. Otwinowski,[27] K. Oyama,[28] P. Sahoo,[126] Y. Pachmayer,[28] M. Pachr,[2] P. Pagano,[95] G. Paić,[90] F. Painke,[21] C. Pajares,[35] S. K. Pal,[9] A. Palmeri,[39] D. Pant,[8] V. Papikyan,[106] G. S. Pappalardo,[39] P. Pareek,[126] W. J. Park,[27] S. Parmar,[4] A. Passfeld,[29] D. I. Patalakha,[64] V. Paticchio,[96] B. Paul,[80] T. Pawlak,[105] T. Peitzmann,[57] H. Pereira Da Costa,[43] E. Pereira De Oliveira Filho,[25] D. Peresunko,[15] C. E. Pérez Lara,[68] A. Pesci,[18] V. Peskov,[33] Y. Pestov,[129] V. Petráček,[2] M. Petran,[2] M. Petris,[26] M. Petrovici,[26] C. Petta,[45] S. Piano,[101] M. Pikna,[71] P. Pillot,[32] O. Pinazza,[36] L. Pinsky,[52] D. B. Piyarathna,[52] M. Płoskoń,[62] M. Planinic,[130,30] J. Pluta,[105] S. Pochybova,[46] P. L. M. Podesta-Lerma,[121] M. G. Poghosyan,[36] E. H. O. Pohjoisaho,[131] B. Polichtchouk,[64] N. Poljak,[30] A. Pop,[26] S. Porteboeuf-Houssais,[40] J. Porter,[62] V. Pospisil,[2] B. Potukuchi,[42] S. K. Prasad,[66] R. Preghenella,[18,17] F. Prino,[5] C. A. Pruneau,[66] I. Pshenichnov,[99] G. Puddu,[77] P. Pujahari,[66] V. Punin,[72] J. Putschke,[66] H. Qvigstad,[49] A. Rachevski,[101] S. Raha,[92] J. Rak,[79] A. Rakotozafindrabe,[43] L. Ramello,[88] R. Raniwala,[132] S. Raniwala,[132] S. S. Räsänen,[131] B. T. Rascanu,[33] D. Rathee,[4] A. W. Rauf,[11] V. Razazi,[77] K. F. Read,[123] J. S. Real,[34] K. Redlich,[133,94] R. J. Reed,[13] A. Rehman,[23] P. Reichelt,[33] M. Reicher,[57] F. Reidt,[36] R. Renfordt,[33] A. R. Reolon,[60] A. Reshetin,[99] F. Rettig,[21] J.-P. Revol,[36] K. Reygers,[28] R. A. Ricci,[134] T. Richert,[83] M. Richter,[49] P. Riedler,[36] W. Riegler,[36] F. Riggi,[45] A. Rivetti,[5] E. Rocco,[57] M. Rodríguez Cahuantzi,[89] A. Rodriguez Manso,[68] K. Røed,[49] E. Rogochaya,[48] S. Rohni,[42] D. Rohr,[21] D. Röhrich,[23] R. Romita,[120] F. Ronchetti,[60] P. Rosnet,[40] A. Rossi,[36] F. Roukoutakis,[100] A. Roy,[126] C. Roy,[51] P. Roy,[80] A. J. Rubio Montero,[61] R. Rui,[76] R. Russo,[54] E. Ryabinkin,[15] A. Rybicki,[47] S. Sadovsky,[64] K. Šafařík,[36] B. Sahlmuller,[33] R. Sahoo,[126] P. K. Sahu,[44] J. Saini,[9] C. A. Salgado,[35] J. Salzwedel,[102] S. Sambyal,[42] V. Samsonov,[56] X. Sanchez Castro,[51] F. J. Sánchez Rodríguez,[121] L. Šándor,[111] A. Sandoval,[53] M. Sano,[59] G. Santagati,[45] D. Sarkar,[9] E. Scapparone,[18] F. Scarlassara,[73] R. P. Scharenberg,[70] C. Schiaua,[26] R. Schicker,[28] C. Schmidt,[27] H. R. Schmidt,[108] S. Schuchmann,[33] J. Schukraft,[36] M. Schulc,[2] T. Schuster,[13] Y. Schutz,[32,36] K. Schwarz,[27] K. Schweda,[27] G. Scioli,[7] E. Scomparin,[5] R. Scott,[123] G. Segato,[73] J. E. Seger,[81] Y. Sekiguchi,[107] I. Selyuzhenkov,[27] J. Seo,[84] E. Serradilla,[61,53] A. Sevcenco,[91] A. Shabetai,[32] G. Shabratova,[48] R. Shahoyan,[36] A. Shangaraev,[64] N. Sharma,[123] S. Sharma,[42] K. Shigaki,[135] K. Shtejer,[54] Y. Sibiriak,[15] S. Siddhanta,[85] T. Siemiarczuk,[94] D. Silvermyr,[37] C. Silvestre,[34] G. Simatovic,[130] R. Singaraju,[9]

R. Singh,[42] S. Singha,[9,127] V. Singhal,[9] B. C. Sinha,[9] T. Sinha,[80] B. Sitar,[71] M. Sitta,[88] T. B. Skaali,[49] K. Skjerdal,[23] R. Smakal,[2] N. Smirnov,[13] R. J. M. Snellings,[57] C. Søgaard,[83] R. Soltz,[1] J. Song,[84] M. Song,[112] F. Soramel,[73] S. Sorensen,[123] M. Spacek,[2] I. Sputowska,[47] M. Spyropoulou-Stassinaki,[100] B. K. Srivastava,[70] J. Stachel,[28] I. Stan,[91] G. Stefanek,[94] M. Steinpreis,[102] E. Stenlund,[83] G. Steyn,[67] J. H. Stiller,[28] D. Stocco,[32] M. Stolpovskiy,[64] P. Strmen,[71] A. A. P. Suaide,[25] T. Sugitate,[135] C. Suire,[86] M. Suleymanov,[11] R. Sultanov,[14] M. Šumbera,[3] T. Susa,[30] T. J. M. Symons,[62] A. Szanto de Toledo,[25] I. Szarka,[71] A. Szczepankiewicz,[36] M. Szymanski,[105] J. Takahashi,[93] M. A. Tangaro,[22] J. D. Tapia Takaki,[136,86] A. Tarantola Peloni,[33] A. Tarazona Martinez,[36] A. Tauro,[36] G. Tejeda Muñoz,[89] A. Telesca,[36] C. Terrevoli,[77] J. Thäder,[27] D. Thomas,[57] R. Tieulent,[82] A. R. Timmins,[52] A. Toia,[31] H. Torii,[107] V. Trubnikov,[19] W. H. Trzaska,[79] T. Tsuji,[107] A. Tumkin,[72] R. Turrisi,[31] T. S. Tveter,[49] J. Ulery,[33] K. Ullaland,[23] A. Uras,[82] G. L. Usai,[77] M. Vajzer,[3] M. Vala,[111,48] L. Valencia Palomo,[86,40] S. Vallero,[28] P. Vande Vyvre,[36] L. Vannucci,[134] J. W. Van Hoorne,[36] M. van Leeuwen,[57] A. Vargas,[89] R. Varma,[8] M. Vasileiou,[100] A. Vasiliev,[15] V. Vechernin,[24] M. Veldhoen,[57] A. Velure,[23] M. Venaruzzo,[76,134] E. Vercellin,[54] S. Vergara Limón,[89] R. Vernet,[137] M. Verweij,[66] L. Vickovic,[104] G. Viesti,[73] J. Viinikainen,[79] Z. Vilakazi,[67] O. Villalobos Baillie,[16] A. Vinogradov,[15] L. Vinogradov,[24] Y. Vinogradov,[72] T. Virgili,[95] Y. P. Viyogi,[9] A. Vodopyanov,[48] M. A. Völkl,[28] K. Voloshin,[14] S. A. Voloshin,[66] G. Volpe,[36] B. von Haller,[36] I. Vorobyev,[24] D. Vranic,[27,36] J. Vrláková,[65] B. Vulpescu,[40] A. Vyushin,[72] B. Wagner,[23] J. Wagner,[27] V. Wagner,[2] M. Wang,[74,32] Y. Wang,[28] D. Watanabe,[59] M. Weber,[52] J. P. Wessels,[29] U. Westerhoff,[29] J. Wiechula,[108] J. Wikne,[49] M. Wilde,[29] G. Wilk,[94] J. Wilkinson,[28] M. C. S. Williams,[18] B. Windelband,[28] M. Winn,[28] C. Xiang,[74] C. G. Yaldo,[66] Y. Yamaguchi,[107] H. Yang,[57] P. Yang,[74] S. Yang,[23] S. Yano,[135] S. Yasnopolskiy,[15] J. Yi,[84] Z. Yin,[74] I.-K. Yoo,[84] I. Yushmanov,[15] V. Zaccolo,[50] C. Zach,[2] A. Zaman,[11] C. Zampolli,[18] S. Zaporozhets,[48] A. Zarochentsev,[24] P. Závada,[109] N. Zaviyalov,[72] H. Zbroszczyk,[105] I. S. Zgura,[91] M. Zhalov,[56] H. Zhang,[74] X. Zhang,[62,74] Y. Zhang,[74] C. Zhao,[49] N. Zhigareva,[14] D. Zhou,[74] F. Zhou,[74] Y. Zhou,[57] H. Zhu,[74] J. Zhu,[74] X. Zhu,[74] A. Zichichi,[17,7] A. Zimmermann,[28] M. B. Zimmermann,[36,29] G. Zinovjev,[19] Y. Zoccarato,[82] M. Zynovyev,[19] and M. Zyzak[33]

(ALICE Collaboration)

[1]*Lawrence Livermore National Laboratory, Livermore, California, USA*
[2]*Faculty of Nuclear Sciences and Physical Engineering, Czech Technical University in Prague, Prague, Czech Republic*
[3]*Nuclear Physics Institute, Academy of Sciences of the Czech Republic, Řežu Prahy, Czech Republic*
[4]*Physics Department, Panjab University, Chandigarh, India*
[5]*Sezione INFN, Turin, Italy*
[6]*Politecnico di Torino, Turin, Italy*
[7]*Dipartimento di Fisica e Astronomia dell'Università and Sezione INFN, Bologna, Italy*
[8]*Indian Institute of Technology Bombay (IIT), Mumbai, India*
[9]*Variable Energy Cyclotron Centre, Kolkata, India*
[10]*Department of Physics, Aligarh Muslim University, Aligarh, India*
[11]*COMSATS Institute of Information Technology (CIIT), Islamabad, Pakistan*
[12]*Korea Institute of Science and Technology Information, Daejeon, South Korea*
[13]*Yale University, New Haven, Connecticut, USA*
[14]*Institute for Theoretical and Experimental Physics, Moscow, Russia*
[15]*Russian Research Centre Kurchatov Institute, Moscow, Russia*
[16]*School of Physics and Astronomy, University of Birmingham, Birmingham, United Kingdom*
[17]*Centro Fermi - Museo Storico della Fisica e Centro Studi e Ricerche "Enrico Fermi", Rome, Italy*
[18]*Sezione INFN, Bologna, Italy*
[19]*Bogolyubov Institute for Theoretical Physics, Kiev, Ukraine*
[20]*Faculty of Engineering, Bergen University College, Bergen, Norway*
[21]*Frankfurt Institute for Advanced Studies, Johann Wolfgang Goethe-Universität Frankfurt, Frankfurt, Germany*
[22]*Dipartimento Interateneo di Fisica 'M. Merlin' and Sezione INFN, Bari, Italy*
[23]*Department of Physics and Technology, University of Bergen, Bergen, Norway*
[24]*V. Fock Institute for Physics, St. Petersburg State University, St. Petersburg, Russia*
[25]*Universidade de São Paulo (USP), São Paulo, Brazil*
[26]*National Institute for Physics and Nuclear Engineering, Bucharest, Romania*
[27]*Research Division and ExtreMe Matter Institute EMMI, GSI Helmholtzzentrum für Schwerionenforschung, Darmstadt, Germany*
[28]*Physikalisches Institut, Ruprecht-Karls-Universität Heidelberg, Heidelberg, Germany*
[29]*Institut für Kernphysik, Westfälische Wilhelms-Universität Münster, Münster, Germany*
[30]*Rudjer Bošković Institute, Zagreb, Croatia*
[31]*Sezione INFN, Padova, Italy*
[32]*SUBATECH, Ecole des Mines de Nantes, Université de Nantes, CNRS-IN2P3, Nantes, France*
[33]*Institut für Kernphysik, Johann Wolfgang Goethe-Universität Frankfurt, Frankfurt, Germany*
[34]*Laboratoire de Physique Subatomique et de Cosmologie, Université Grenoble-Alpes, CNRS-IN2P3, Grenoble, France*

[35]*Departamento de Física de Partículas and IGFAE, Universidad de Santiago de Compostela, Santiago de Compostela, Spain*

[36]*European Organization for Nuclear Research (CERN), Geneva, Switzerland*

[37]*Oak Ridge National Laboratory, Oak Ridge, Tennessee, USA*

[38]*Physics Department, University of Cape Town, Cape Town, South Africa*

[39]*Sezione INFN, Catania, Italy*

[40]*Laboratoire de Physique Corpusculaire (LPC), Clermont Université, Université Blaise Pascal, CNRS-IN2P3, Clermont-Ferrand, France*

[41]*Gangneung-Wonju National University, Gangneung, South Korea*

[42]*Physics Department, University of Jammu, Jammu, India*

[43]*Commissariat à l'Energie Atomique, IRFU, Saclay, France*

[44]*Institute of Physics, Bhubaneswar, India*

[45]*Dipartimento di Fisica e Astronomia dell'Università and Sezione INFN, Catania, Italy*

[46]*Wigner Research Centre for Physics, Hungarian Academy of Sciences, Budapest, Hungary*

[47]*The Henryk Niewodniczanski Institute of Nuclear Physics, Polish Academy of Sciences, Cracow, Poland*

[48]*Joint Institute for Nuclear Research (JINR), Dubna, Russia*

[49]*Department of Physics, University of Oslo, Oslo, Norway*

[50]*Niels Bohr Institute, University of Copenhagen, Copenhagen, Denmark*

[51]*Institut Pluridisciplinaire Hubert Curien (IPHC), Université de Strasbourg, CNRS-IN2P3, Strasbourg, France*

[52]*University of Houston, Houston, Texas, USA*

[53]*Instituto de Física, Universidad Nacional Autónoma de México, Mexico City, Mexico*

[54]*Dipartimento di Fisica dell'Università and Sezione INFN, Turin, Italy*

[55]*St. Petersburg State Polytechnical University, St. Petersburg, Russia*

[56]*Petersburg Nuclear Physics Institute, Gatchina, Russia*

[57]*Institute for Subatomic Physics of Utrecht University, Utrecht, Netherlands*

[58]*Department of Physics, Gauhati University, Guwahati, India*

[59]*University of Tsukuba, Tsukuba, Japan*

[60]*Laboratori Nazionali di Frascati, INFN, Frascati, Italy*

[61]*Centro de Investigaciones Energéticas Medioambientales y Tecnológicas (CIEMAT), Madrid, Spain*

[62]*Lawrence Berkeley National Laboratory, Berkeley, California, USA*

[63]*Moscow Engineering Physics Institute, Moscow, Russia*

[64]*SSC IHEP of NRC Kurchatov Institute, Protvino, Russia*

[65]*Faculty of Science, P.J. Šafárik University, Košice, Slovakia*

[66]*Wayne State University, Detroit, Michigan, USA*

[67]*iThemba LABS, National Research Foundation, Somerset West, South Africa*

[68]*Nikhef, National Institute for Subatomic Physics, Amsterdam, Netherlands*

[69]*Institut für Informatik, Johann Wolfgang Goethe-Universität Frankfurt, Frankfurt, Germany*

[70]*Purdue University, West Lafayette, Indiana, USA*

[71]*Faculty of Mathematics, Physics and Informatics, Comenius University, Bratislava, Slovakia*

[72]*Russian Federal Nuclear Center (VNIIEF), Sarov, Russia*

[73]*Dipartimento di Fisica e Astronomia dell'Università and Sezione INFN, Padova, Italy*

[74]*Central China Normal University, Wuhan, China*

[75]*Sección Física, Departamento de Ciencias, Pontificia Universidad Católica del Perú, Lima, Peru*

[76]*Dipartimento di Fisica dell'Università and Sezione INFN, Trieste, Italy*

[77]*Dipartimento di Fisica dell'Università and Sezione INFN, Cagliari, Italy*

[78]*Centro de Aplicaciones Tecnológicas y Desarrollo Nuclear (CEADEN), Havana, Cuba*

[79]*University of Jyväskylä, Jyväskylä, Finland*

[80]*Saha Institute of Nuclear Physics, Kolkata, India*

[81]*Physics Department, Creighton University, Omaha, Nebraska, USA*

[82]*Université de Lyon, Université Lyon 1, CNRS/IN2P3, IPN-Lyon, Villeurbanne, France*

[83]*Division of Experimental High Energy Physics, University of Lund, Lund, Sweden*

[84]*Pusan National University, Pusan, South Korea*

[85]*Sezione INFN, Cagliari, Italy*

[86]*Institut de Physique Nucléaire d'Orsay (IPNO), Université Paris-Sud, CNRS-IN2P3, Orsay, France*

[87]*Centro de Investigación y de Estudios Avanzados (CINVESTAV), Mexico City and Mérida, Mexico*

[88]*Dipartimento di Scienze e Innovazione Tecnologica dell'Università del Piemonte Orientale and Gruppo Collegato INFN, Alessandria, Italy*

[89]*Benemérita Universidad Autónoma de Puebla, Puebla, Mexico*

[90]*Instituto de Ciencias Nucleares, Universidad Nacional Autónoma de México, Mexico City, Mexico*

[91]*Institute of Space Science (ISS), Bucharest, Romania*

[92]*Bose Institute, Department of Physics and Centre for Astroparticle Physics and Space Science (CAPSS), Kolkata, India*

[93]*Universidade Estadual de Campinas (UNICAMP), Campinas, Brazil*

[94]*National Centre for Nuclear Studies, Warsaw, Poland*

[95]*Dipartimento di Fisica "E.R. Caianiello" dell'Università and Gruppo Collegato INFN, Salerno, Italy*

[96]*Sezione INFN, Bari, Italy*

[97]*Sezione INFN, Rome, Italy*

[98]*University of Liverpool, Liverpool, United Kingdom*

[99]*Institute for Nuclear Research, Academy of Sciences, Moscow, Russia*

[100]*Physics Department, University of Athens, Athens, Greece*

[101]*Sezione INFN, Trieste, Italy*

[102]*Department of Physics, Ohio State University, Columbus, Ohio, USA*

[103]*Chicago State University, Chicago, USA*

[104]*Technical University of Split FESB, Split, Croatia*

[105]*Warsaw University of Technology, Warsaw, Poland*

[106]*A.I. Alikhanyan National Science Laboratory (Yerevan Physics Institute) Foundation, Yerevan, Armenia*

[107]*University of Tokyo, Tokyo, Japan*

[108]*Eberhard Karls Universität Tübingen, Tübingen, Germany*

[109]*Institute of Physics, Academy of Sciences of the Czech Republic, Prague, Czech Republic*

[110]*Department of Physics, Sejong University, Seoul, South Korea*

[111]*Institute of Experimental Physics, Slovak Academy of Sciences, Košice, Slovakia*

[112]*Yonsei University, Seoul, South Korea*

[113]*KTO Karatay University, Konya, Turkey*

[114]*Zentrum für Technologietransfer und Telekommunikation (ZTT), Fachhochschule Worms, Worms, Germany*

[115]*Department of Applied Physics, Aligarh Muslim University, Aligarh, India*

[116]*California Polytechnic State University, San Luis Obispo, California, USA*

[117]*The University of Texas at Austin, Physics Department, Austin, Texas, USA*

[118]*Suranaree University of Technology, Nakhon Ratchasima, Thailand*

[119]*Vestfold University College, Tonsberg, Norway*

[120]*Nuclear Physics Group, STFC Daresbury Laboratory, Daresbury, United Kingdom*

[121]*Universidad Autónoma de Sinaloa, Culiacán, Mexico*

[122]*M.V. Lomonosov Moscow State University, D.V. Skobeltsyn Institute of Nuclear Physics, Moscow, Russia*

[123]*University of Tennessee, Knoxville, Tennessee, USA*

[124]*Dipartimento di Fisica dell'Università 'La Sapienza' and Sezione INFN Rome, Italy*

[125]*University of Belgrade, Faculty of Physics and "Vinča" Institute of Nuclear Sciences, Belgrade, Serbia*

[126]*Indian Institute of Technology Indore, Indore (IITI), India*

[127]*National Institute of Science Education and Research, Bhubaneswar, India*

[128]*Permanent Address: Konkuk University, Seoul, Korea*

[129]*Budker Institute for Nuclear Physics, Novosibirsk, Russia*

[130]*University of Zagreb, Zagreb, Croatia*

[131]*Helsinki Institute of Physics (HIP), Helsinki, Finland*

[132]*Physics Department, University of Rajasthan, Jaipur, India*

[133]*Institute of Theoretical Physics, University of Wroclaw, Wroclaw, Poland*

[134]*Laboratori Nazionali di Legnaro, INFN, Legnaro, Italy*

[135]*Hiroshima University, Hiroshima, Japan*

[136]*University of Kansas, Lawrence, Kansas, USA*

[137]*Centre de Calcul de l'IN2P3, Villeurbanne, France*

[†]alice-publications@cern.ch

[‡]Deceased.